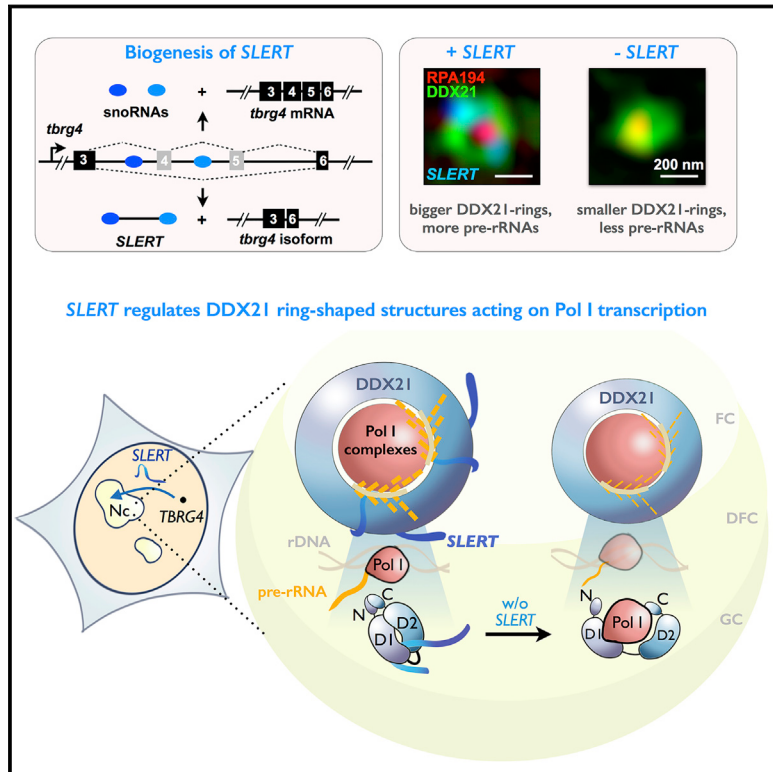


# SLERT Regulates DDX21 Rings Associated with Pol I Transcription

## Graphical Abstract



## Highlights

- **SLERT** is a box H/ACA snoRNA-ended lncRNA that enhances pre-rRNA transcription
- DDX21 forms ring-shaped structures surrounding Pol I and inhibits Pol I transcription
- **SLERT** binds to DDX21 and modulates DDX21 rings to evict their suppression on Pol I
- **SLERT-DDX21** interactions regulate differential expression of rDNAs

## Authors

Yu-Hang Xing, Run-Wen Yao,  
Yang Zhang, ..., Rui Dong, Li Yang,  
Ling-Ling Chen

## Correspondence

linglingchen@sibcb.ac.cn

## In Brief

A long non-coding RNA promotes pre-ribosomal RNA transcription by loosening the ring-shaped structure surrounding multiple RNA Pol I complexes formed by RNA helicase DDX21.



# SLERT Regulates DDX21 Rings Associated with Pol I Transcription

Yu-Hang Xing,<sup>1,5</sup> Run-Wen Yao,<sup>1,5</sup> Yang Zhang,<sup>1,5</sup> Chun-Jie Guo,<sup>1</sup> Shan Jiang,<sup>1</sup> Guang Xu,<sup>1</sup> Rui Dong,<sup>2</sup> Li Yang,<sup>2,3,4</sup> and Ling-Ling Chen<sup>1,3,4,6,\*</sup>

<sup>1</sup>State Key Laboratory of Molecular Biology, Shanghai Key Laboratory of Molecular Andrology, CAS Center for Excellence in Molecular Cell Science, Shanghai Institute of Biochemistry and Cell Biology, Chinese Academy of Sciences, University of Chinese Academy of Sciences, 320 Yueyang Road, Shanghai 200031, China

<sup>2</sup>Key Laboratory of Computational Biology, CAS-MPG Partner Institute for Computational Biology, Shanghai Institutes for Biological Sciences, Chinese Academy of Sciences, University of Chinese Academy of Sciences, 320 Yueyang Road, Shanghai 200031, China

<sup>3</sup>School of Life Science and Technology, ShanghaiTech University, 100 Haik Road, Shanghai 201210, China

<sup>4</sup>Senior author

<sup>5</sup>These authors contributed equally

<sup>6</sup>Lead Contact

\*Correspondence: linglingchen@sibcb.ac.cn  
<http://dx.doi.org/10.1016/j.cell.2017.04.011>

## SUMMARY

Dysregulated rRNA synthesis by RNA polymerase I (Pol I) is associated with uncontrolled cell proliferation. Here, we report a box H/ACA small nucleolar RNA (snoRNA)-ended long noncoding RNA (lncRNA) that enhances pre-rRNA transcription (*SLERT*). *SLERT* requires box H/ACA snoRNAs at both ends for its biogenesis and translocation to the nucleolus. Deletion of *SLERT* impairs pre-rRNA transcription and rRNA production, leading to decreased tumorigenesis. Mechanistically, *SLERT* interacts with DEAD-box RNA helicase DDX21 via a 143-nt non-snoRNA sequence. Super-resolution images reveal that DDX21 forms ring-shaped structures surrounding multiple Pol I complexes and suppresses pre-rRNA transcription. Binding by *SLERT* allosterically alters individual DDX21 molecules, loosens the DDX21 ring, and evicts DDX21 suppression on Pol I transcription. Together, our results reveal an important control of ribosome biogenesis by *SLERT* lncRNA and its regulatory role in DDX21 ring-shaped arrangements acting on Pol I complexes.

## INTRODUCTION

Long noncoding RNAs (lncRNAs) are important modulators of nuclear organization and function. They are responsible for nuclear structure integrity and can regulate the expression of either nearby genes or of genes elsewhere in cells via multiple mechanisms, including through recruiting transcription factors or chromatin-modifying complexes to their DNA targets, by forming ribonucleoprotein complexes, by acting as decoys to sequester RNA binding proteins, or by directly interacting with RNAs and DNAs by base-pairing (Chen, 2016).

The nucleolus is a non-membrane-bound nuclear organelle found in all eukaryotes and best known for its role in coordinating ribosome biogenesis. Nucleoli form around specific chromosomal features called nucleolar organizing regions (NORs) that contain arrays of rDNAs. In the human genome, there are >400 copies of rDNAs with interspersed active and inactive gene repeats distributed along five chromosomes, and only some rDNA genes remain active (Boisvert et al., 2007). How specific rDNA genes within a NOR cluster remain transcriptionally inert is unclear. The active rDNAs are transcribed by RNA polymerase I (Pol I) to produce pre-rRNAs that undergo modification and processing to remove external transcribed spacers (ETSs) and internal transcribed spacers (ITSs) to yield mature 18S, 5.8S, and 28S rRNAs (McStay, 2016). Pol I activity is a key determinant for the level of ribosome production and controls cell growth and proliferation. Uncontrolled rRNA synthesis by Pol I is associated with aberrant cell proliferation (Nguyen et al., 2015; Peltonen et al., 2014).

Although lncRNAs are suspected to impact many cellular processes, few have been reported to be involved in nucleolar functions or Pol I transcription regulation. In mouse cells, two rDNA-produced lncRNAs were shown to regulate rRNA synthesis at the chromatin level (Schmitz et al., 2010; Bierhoff et al., 2014). The promoter-associated RNAs (pRNAs) are produced from rDNA promoters and can trigger DNA methylation and silence rRNA genes depending on the nucleolar remodeling complex (Schmitz et al., 2010). The Papas (promoter and pre-rRNA antisense) lncRNA triggers H4K20me3 at rDNAs by binding the H4K20 methyltransferase Suv4-20h2 to silence rDNAs in quiescent cells (Bierhoff et al., 2014). However, whether pRNA and Papas play similar roles in human and whether the Pol I activity is controlled by regulatory RNAs are unknown.

While a large proportion of lncRNAs look like mRNAs, a number of lncRNAs are processed in unusual ways (Chen, 2016). The excised intron-derived sno-lncRNAs are formed when one intron contains two small nucleolar RNA (snoRNA) genes (Yin et al., 2012). After splicing, the sequences between the snoRNAs are not degraded, leading to the accumulation of lncRNAs flanked by snoRNA sequences but lacking 5' caps and 3' poly (A) tails. Both box C/D and box H/ACA snoRNA-ended lncRNAs are

expressed in mammals and their expression is associated with alternative splicing (Zhang et al., 2014). Here, we report the biogenesis and function of a box H/ACA snoRNA-ended sno-lncRNA, referred to *SLERT* (snoRNA-ended lncRNA enhances pre-ribosomal RNA transcription). *SLERT* is different from reported Prader-Willi Syndrome (PWS) sno-lncRNAs and plays a crucial role in rRNA biogenesis by dislodging a previously unknown clamp of DDX21 ring-shaped arrangements on Pol I complexes, thereby liberating Pol I for active rRNA transcription.

## RESULTS

### Box H/ACA snoRNAs Are Required for *SLERT* lncRNA Formation and Nucleolar Localization

Non-polyadenylated (non-poly(A)) RNA sequencing (RNA-seq) (Yang et al., 2011) allowed us to identify sno-lncRNAs (Yin et al., 2012; Zhang et al., 2014). One box H/ACA snoRNA-ended lncRNA, *SLERT*, is robustly expressed in human embryonic stem cells (hESCs) H9 and ovarian carcinoma cells PA1 with ~210 or 156 copies per cell, respectively (Figures 1A, S1A, and S1B). It is also highly expressed in many other examined human cell lines (Figure S1C).

*SLERT* is 694 nt in length and contains SNORA5A and SNORA5C at its ends (Figure 1A). It is produced from the human *TBRG4* locus via skipping of exons 4 and 5 (Figure 1B) that leads to both SNORA5A and SNORA5C embedded within one intron, thereby producing *SLERT* from this large and alternatively spliced intron (Figure 1C). The shorter isoform of *TBRG4* with skipped exons could be detected in PA1 cells (Figure S1D) with a relatively rapid degradation rate (Figure S1E). Thus, at the *TBRG4* locus, alternative splicing of the *TBRG4* pre-mRNA produces either *TBRG4* and two individual snoRNAs or *SLERT* and an alternatively spliced *TBRG4* isoform with exons 4 and 5 skipped (Figure 1C). The unusual processing of *SLERT* indicates that its expression regulation may occur at multiple levels.

DKC1 is one key component of the box H/ACA snoRNP (Watkins and Bohnsack, 2012). *SLERT* could be efficiently immunoprecipitated with anti-DKC1 antibodies, while control RNAs including a box C/D snoRNA-ended lncRNA or *XIST*, could not (Figure S1F), supporting the notion that *SLERT* is ended with box H/ACA snoRNPs. To dissect the mechanism of *SLERT* processing, we constructed a set of *SLERT* mutant vectors in which the loops or the box H motifs of the two snoRNA ends were sequentially deleted (Figure 1D). These plasmids were individually transfected to HeLa cells, which have the relatively low level of endogenous *SLERT* (Figure S1C), followed by northern blotting (NB) to detect *SLERT* processed from each mutant. Results clearly showed that both H motifs and two outside loops of both box H/ACA snoRNAs were crucial for *SLERT* processing (Figure 1D, 1, 2, 6, and 7), while effects of deleting inside loops were minor on *SLERT* formation (Figure 1D, 3 and 5). Furthermore, deletion of the box ACA motif at the 3' end of *SLERT* (Figure 1D, 8), but not the one within *SLERT* (Figure 1D, 4), impaired its processing. Thus, *SLERT* processing requires essential motifs of each box H/ACA snoRNA at its end that is able to form the intact or partial snoRNP complex. Such H/ACA snoRNPs at the ends protect the intronic sequence from exonuclease trimming after splicing, leading to *SLERT* formation.

It is becoming increasingly clear that the function of lncRNAs is associated with their unique subcellular localization patterns (Chen, 2016). Subcellular fractionation followed by RT-PCR in PA1 cells revealed that *SLERT* mainly accumulated in the nucleolus (Figure 1E). Co-staining of *SLERT* by RNA fluorescence in situ hybridization (FISH) and the nucleolar marker protein nucleolin showed that *SLERT* almost exclusively localized to nucleoli in PA1 (Figure 1F), CRL-5807, and H9 cells (Figure S1G) that have high *SLERT* levels (Figure S1C). Of note, its nucleolar localization could also be detected in HeLa cells that have relatively low *SLERT* expression (Figure S1G).

Interestingly, the *TBRG4* gene locus, from which *SLERT* is generated, is located at a distance from nucleoli in cells (Figure 1G). This observation indicates that a specific mechanism is associated with *SLERT* translocation to the nucleolus. It is known that most snoRNAs localize to the nucleolus or traffic through the nucleolus during their life cycles (Boisvert et al., 2007); thus, it is tempting to speculate that snoRNAs at the ends of *SLERT* are required for its nucleolar translocation. We constructed three vectors that expressed wild-type (WT) or mutants of *SLERT* (WT-*SLERT*<sup>MUT</sup> and *egfp*-*SLERT*) (Figure 1H). The WT-*SLERT*<sup>MUT</sup> contains deletion of the two inside loops of snoRNAs so that a mutant *SLERT* carrying the full internal sequence, but without intact snoRNA ends, was generated. In the *egfp*-*SLERT* mutant, the internal sequence of *SLERT* was replaced with a fragment of *egfp* so that a mutant *egfp*-*SLERT* was produced with intact snoRNA ends and an *egfp* insertion (Figure 1H). Transfection of each plasmid, followed by detection of *SLERT* RNA and nucleolin, showed that *egfp*-*SLERT* mainly localized to the nucleolus while the WT-*SLERT*<sup>MUT</sup> largely distributed in the nucleoplasm (Figure 1H). These results support the view that *SLERT* requires its box H/ACA snoRNA ends for translocation to the nucleolus.

### *SLERT* Promotes Pre-rRNA Transcription via Its Non-snoRNA Region in the Nucleolus

Because *SLERT* mainly accumulates to the nucleolus, we asked whether *SLERT* would have any measurable effect on rRNA biogenesis. We generated *SLERT* knockout (KO) PA1 cells by CRISPR/CAS9 without affecting its parental *TBRG4* mRNA expression. To do so, we designed two single-guide RNAs (sgRNAs) that individually target the minimal sequence that is required for *SLERT* formation, the box H of each snoRNA (Figures 1D and 2A). A number of clones were obtained with disrupted *SLERT* expression (Figures S1H and S1I), and two clones were used in this study (Figures 2A and 2B). As expected, *TBRG4* protein levels were not affected in these *SLERT* KO cells (Figure 2C), excluding potential roles that *TBRG4* may play in the observable *SLERT* phenotypes. It should be noted that one of the two snoRNAs was also depleted in each corresponding *SLERT* KO single clone (Figure 2B). In these *SLERT* KO cell lines, steady-state levels of 47S pre-rRNA were remarkably reduced (Figure 2D). Similar results were also observed in other *SLERT* KO cell lines (Figure S1I). In addition, *SLERT* depletion resulted in decreased 28S and 18S rRNAs by comparing RNAs collected from an equal number of cells in control and *SLERT* KO cells (Figures 2B and 2D). The reduction of mature rRNAs was further evidenced by decreased 40S and 60S ribosomal subunits

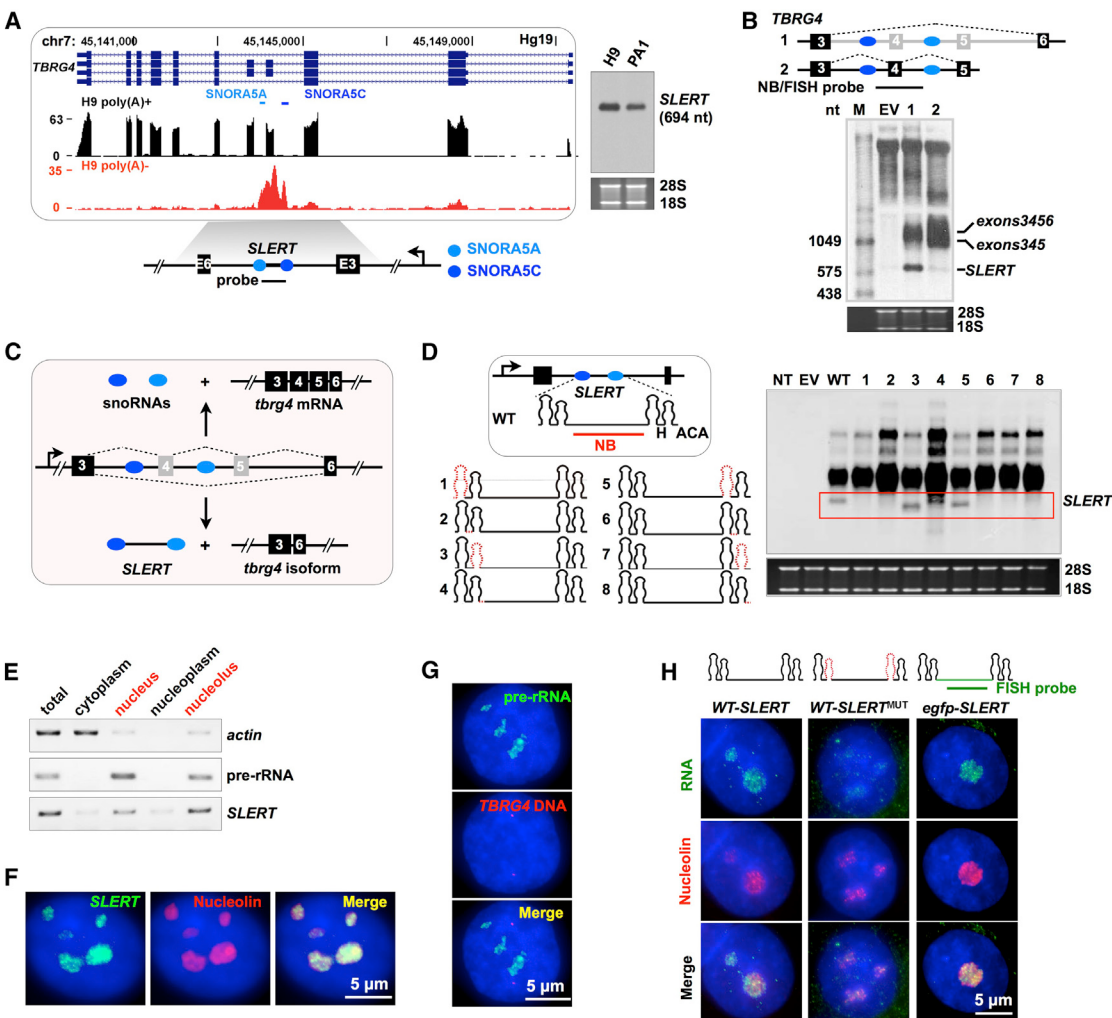


**Figure 1.** Box H/ACA snoRNAs Are Required for SLERT Formation and Nucleolar Localization

(A) The human TBRG4 locus. Left: RNA-seq data was generated from poly(A)<sup>+</sup> RNA-seq (black) and poly(A) RNA-seq (red) in H9 cells. SLERT (red) is ended with SNORAS5A and SNORAS5C. Right: NB detected SLERT in H9 and PA1 cells. See also Figures S1A–S1C.

(B) Recapitulation of SLERT processing. Top: a schematic drawing of SLERT and its flanking sequences cloned into pcDNA3 for SLERT expression; 1 includes exons 3–6, whereas 2 includes exons 3–5 of TBRG4 and their flanking introns containing SLERT. Bottom: SLERT formation requires exon skipping of exons 4 and 5 of TBRG4 shown by NB. Equal amount of total RNA isolated from HeLa cells transfected with each indicated plasmid was resolved on agarose gels for NB with an antisense probe (black bar). Note that the NB probe for SLERT also recognizes exon 4 of TBRG4 mRNA and both spliced linear mRNAs and SLERT could be detected. M, RNA marker; EV, empty vector. See also Figure S1D.

(C) A schematic view of SLERT processing. See also Figure S1E.

(D) SLERT processing requires intact H/ACA boxes at both ends. Left: a schematic drawing of wild-type (WT) SLERT (clone 1 in B) and deletions of box H/ACA (clones 1–8, red dashed lines). Right: NB of SLERT clones expressed in HeLa cells. NT, no transfection. See also Figure S1F.

(E) SLERT accumulates to the nucleolus. Total RNA from PA1 cells was separated into cytoplasmic, nuclear, nucleoplasmic, and nucleolar fractions and analyzed by semiquantitative RT-PCR.

(F) SLERT localizes to the nucleolus. Co-staining of SLERT (green) and nucleolin (red) in PA1 cells. See also Figure S1E.

(G) The TBRG4 locus localizes at a distance to the nucleolus, revealed by double FISH in PA1 cells. Green, pre-rRNA; red, TBRG4 DNA locus.

(H) SLERT requires its box H/ACA snoRNA ends to translocate to the nucleolus. HeLa cells were transfected with each indicated plasmid, followed by co-staining of WT-SLERT, WT-SLERT<sup>MUT</sup>, or egfp-SLERT (green) and nucleolin (red). Probes for WT-SLERT and WT-SLERT<sup>MUT</sup> are shown in (B) and egfp-SLERT is shown as a green bar. See also Figure S1G.

extracted from SLERT KO cells (Figure 2E), confirming an important role of SLERT in rRNA biogenesis.

rRNA production results from both rRNA transcription and processing. To dissect at which level SLERT regulates pre-rRNA abundance, we set up assays to discriminate 47S pre-

rRNA transcription from its processing. We treated PA1 cells with 5-fluorouracil (5-FU) to stop pre-rRNA processing (Zhang et al., 2011) and then pulse-chased with 4-thiouridine (4sU) to detect nascent pre-rRNA in control and SLERT-depleted cells (Zhang et al., 2016). Nascent pre-rRNA was dramatically

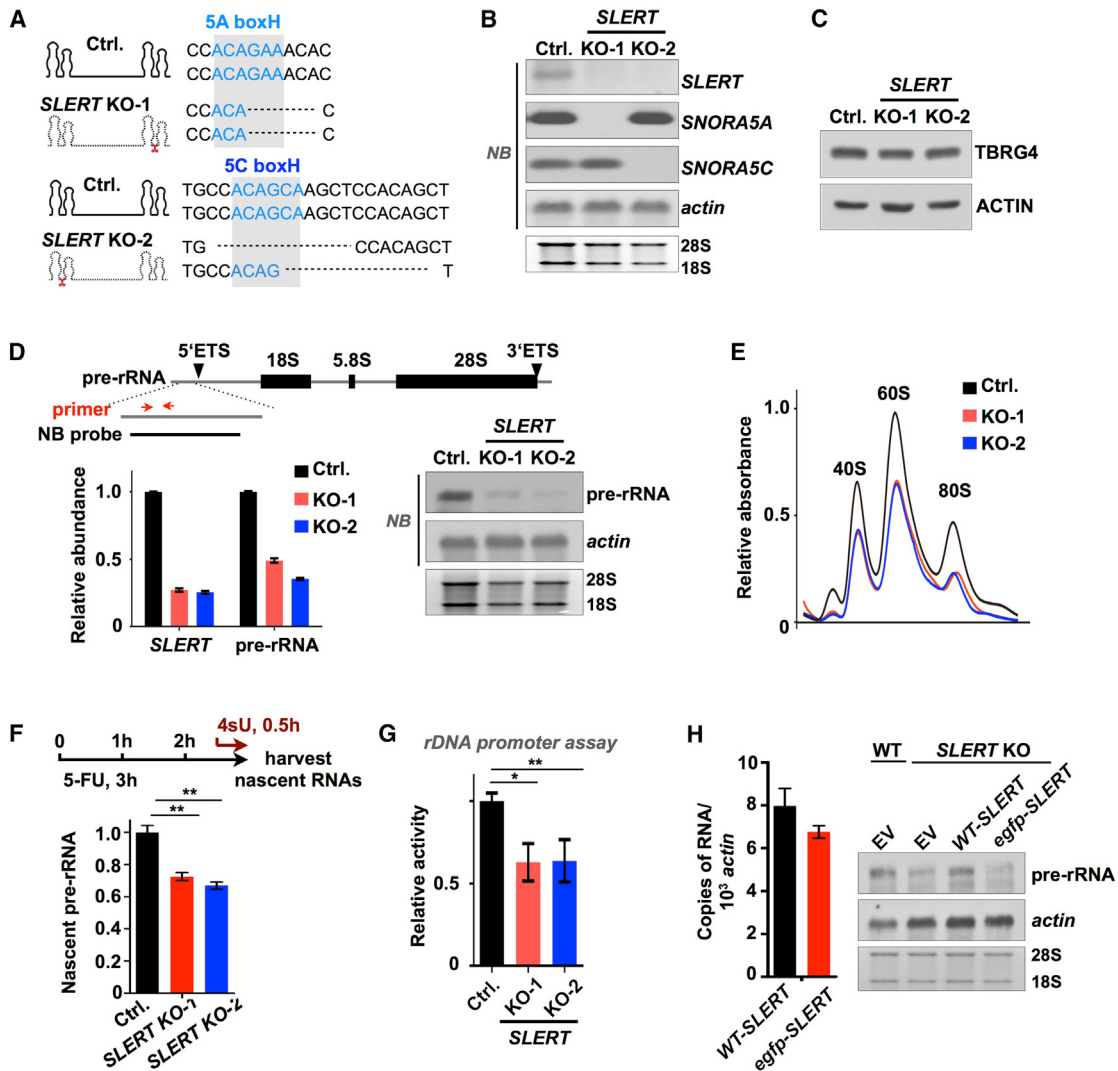


**Figure 2. SLERT Enhances Pre-rRNA Transcription in the Nucleolus**

(A) SLERT KO by CRISPR/CAS9 in PA1 cells. Each sgRNA targets the box H of each snoRNA (see Figure 1D). Control PA1 cells (Ctrl.), transfected PX330 empty vector. Two single clones carrying the indicated deletion are used in this study. See also Figures S1H and S1I.

(B) SLERT KO leads to reduced 28S and 18S rRNAs in PA1 cells. Total RNA collected from equal number of cells across samples was loaded for NB, and actin mRNA was used as a control. See also Figure S1J.

(C) SLERT KO by CRISPR/CAS9 has no detectable effect on TBRG4, revealed by WB.

(D) SLERT KO reduces the steady-state level of pre-rRNA, revealed by qRT-PCR (left) and NB (right). For qRT-PCR, data were normalized to actin. For NB, total RNA collected from equal number of cells across samples was loaded. Primers and NB probe recognize human rDNA sequences from +307 to +442 that map uniquely to 47S pre-rRNA (Feng et al., 2010). See also Figure S1I.

(E) SLERT KO impairs rRNA biogenesis. Cell lysates from control and SLERT KO cells were separated from gradient 10% to 45% sucrose density and measured absorbance under 254 nm UV light. Three major absorption peaks represent 40S, 60S ribosomal subunit, and 80S ribosome.

(F) Nascent pre-rRNA transcription is decreased in SLERT KO cells. SLERT KO cells were pretreated with 5-FU for 3 hr to stop pre-rRNA processing and 4sU labeling in the last 0.5 hr, followed by collection of nascent pre-rRNA for qRT-PCR, normalized to nascent actin pre-mRNA.

(G) Luciferase reporter assay of rDNA promoter in SLERT KO cells. The rDNA promoter and an IRES sequence were cloned upstream of the promoter-less Firefly luciferase coding region. Data were normalized to Renilla luciferase and presented with respect to control cells set to a value of 1.

(H) The internal sequence of SLERT promotes pre-rRNA transcription. Left: qRT-PCR revealed the relative level of WT- and egfp-SLERT in SLERT KO cells (normalized to actin mRNA). Right: OE of WT-, but not egfp-SLERT, in SLERT KO cells rescued pre-rRNA production. For NB, total RNA collected from equal number of cells across samples was loaded. See also Figure S1J.

In (D) and (F)–(H), error bars represent SD in triplicate experiments. \*p < 0.05 and \*\*p < 0.01 (Student's t test).

decreased in *SLERT* KO cells compared to that in control cells (Figure 2F), suggesting that *SLERT* regulation largely occurs at the transcriptional level. In agreement with this result, the luciferase reporter assay of the rDNA promoter also showed marked decreases of luciferase in *SLERT* KO cells (Figure 2G). In addition, overexpression (OE) of *WT-SLERT*, but not *egfp-SLERT* mutant (Figure 1H), enhanced pre-rRNA expression (Figure S1J). Similarly, *WT-SLERT*, but not *egfp-SLERT* OE in *SLERT* KO cells, rescued pre-rRNA production (Figure 2H). Together, these results suggest that the internal region of *SLERT* is essential for promoting rRNA transcription, and *SLERT* is capable of interfering with Pol I transcription via its non-snoRNA sequence.

### The Non-snoRNA Internal Sequence of *SLERT* Interacts with DDX21 in the Nucleolus

To gain insight into the mechanism of *SLERT*-enhanced rRNA transcription, we fused the tRNA scaffold to a Streptavidin aptamer (tRSA) (Iioka et al., 2011) with the full-length *SLERT* (tRSA-*SLERT*) to identify *SLERT*-associated proteins (Figure 3A). tRSA-*SLERT* or tRSA alone was incubated with PA1 cell lysates, and tRSA-*SLERT*-enriched bands were subjected to mass spectrometry (MS) (Figures 3B and S2A). Among identified proteins by MS, one specific one was DDX21 (Figure 3B). Reciprocal immunoprecipitation using DDX21 antibodies to detect its associated RNAs under both native and formaldehyde cross-linking conditions confirmed that DDX21 interacted with *SLERT* (Figure 3C). Immunofluorescence (IF) images also showed the colocalization of DDX21 and *SLERT* in the nucleolus (Figure 3D). Interestingly, some other proteins (e.g., hnRNP U) were also found to affect rRNA biogenesis (Figures S2B and S2C); however, they non-specifically bound to both tRSA-*SLERT* and tRSA (Figure 3B), and they were also not located to the nucleolus (Figures S2B and S2C), thus they were excluded from further analyses.

DDX21 is a DEAD-box RNA helicase and known to be involved in multiple steps of ribosome biogenesis (Calo et al., 2015; Holmström et al., 2008; Sloan et al., 2015). We asked how *SLERT* interacts with DDX21. First, we found that the full-length and the internal non-snoRNA sequence of *SLERT* showed comparable binding affinity to DDX21 (Figure 3E). We then made a series of *SLERT* fragments to dissect the binding capacity of different regions of *SLERT* with DDX21. Each digoxin (Dig)-labeled *SLERT* fragment was incubated with the partially purified DDX21, and eluted RNAs were resolved on denaturing PAGE gel followed by immunoblotting with anti-Dig antibodies. We found that the internal sequence exhibited similar binding capability to full-length *SLERT* (Figure 3F, lanes 1 and 2), confirming results obtained from tRSA precipitation assays (Figure 3E). Importantly, we identified a 143-nt fragment located in the 3' region of *SLERT* (*SLERT*<sub>143</sub>) to specifically interact with DDX21 (Figure 3, lane 9), whereas SNORA5C and SNORA5A exhibited, at best, limited binding to DDX21 (Figure 3F, lanes 3 and 4). Further splitting the 143-nt sequence to smaller fragments eliminated DDX21 binding (Figure 3F, lanes 10 and 11), indicating that this 143-nt sequence may fold into a higher order structure that is required for DDX21 binding. To further test the interaction between *SLERT* and DDX21, we conducted electrophoretic mobility shift assays (EMSA) between in vitro transcribed (IVT) *SLERT*<sub>143</sub> and purified His-DDX21 (Figure S2D). As expected, EMSAs revealed

a direct interaction between DDX21 and *SLERT*<sub>143</sub>. *SLERT*<sub>143</sub> could bind to multimeric DDX21 when the protein was at high concentrations (Figure 3G). These analyses reveal that the non-snoRNA region of *SLERT* directly interacts with DDX21, consistent with the notion that the internal sequence of *SLERT* is responsible for promoting rRNA transcription (Figure 2), and snoRNA ends are required for nucleolar translocation (Figure 1H).

### DDX21 Forms Ring-Shaped Arrangements

To decipher the function of DDX21 in the nucleolus, we examined DDX21 subcellular localization in great detail. Standard IF of DDX21 and nucleolin in fixed PA1 cells visualized by wide-field microscopy revealed that DDX21 was co-localized with nucleolin and enriched in the nucleolus (Figure 4A). Fusion of EGFP to the N terminus of DDX21 and imaging EGFP-DDX21 in live cells also revealed a remarkable nucleolar accumulation of DDX21 (Figure S3A). Importantly, application of super-resolution structured illumination microscopy (SIM) unexpectedly revealed a striking organization pattern of DDX21 in the nucleolus: all detectable DDX21 forms donut-like ring structures with diameters at ~400 nm (Figure 4B; Movie S1). On average, 60 DDX21 rings per cell were observed in fixed PA1 cells (Figure 4C). To exclude artifacts that might be caused by antibodies or fixation conditions, we also visualized DDX21 localization in live cells. Using a live-cell deconvolution imaging system (lateral resolution ~250 nm), we observed that both N-terminal fused EGFP-DDX21 and C-terminal fused DDX21-mCherry exhibited donut-like arrangements in the nucleolus in live PA1 (Figures S3B and S3C; Movie S2) and HeLa (Figure S3D) cells. Together, these observations reveal that DDX21 is mainly located to the nucleolus and forms specific spatial arrangements.

### DDX21 Ring-Shaped Arrangements Surround Pol I and Suppress Pol I Transcription

To dissect how DDX21 and its ring-like arrangements act in the nucleolus, we treated PA1 cells with actinomycin D (AMD) or 5-FU to inhibit rRNA transcription or processing, respectively. The ring pattern of DDX21 was completely disrupted when Pol I transcription was repressed by different concentrations of AMD for 3 hr (50 ng/mL, Figure 4D; 1 µg/mL and 10 µg/mL, Figure S3E). In contrast, no detectable effect by SIM could be observed when pre-rRNA processing was blocked (Figure 4D). The disruption of DDX21 ring-like structures was also observed in live cells expressing EGFP-DDX21 after 50 ng/mL AMD treatment (Figure S3F). These results reveal that the DDX21 ring-shaped arrangements are coupled to rRNA transcription but not to pre-rRNA processing.

These observations (Figures 4D, S3E, and S3F) prompted us to examine the detailed spatial relationship between DDX21 rings and Pol I complexes. SIM observations of DDX21 and RPA194, the largest subunit of the Pol I complex, revealed a striking localization pattern between these two proteins: almost all detectable RPA194 is located in the halo center of DDX21 rings (Figure 4E). Inhibition of Pol I transcription by AMD completely impaired DDX21 ring-shaped arrangements surrounding Pol I complexes (Figure 4D). Live cell imaging also confirmed the unique localization pattern between DDX21 and

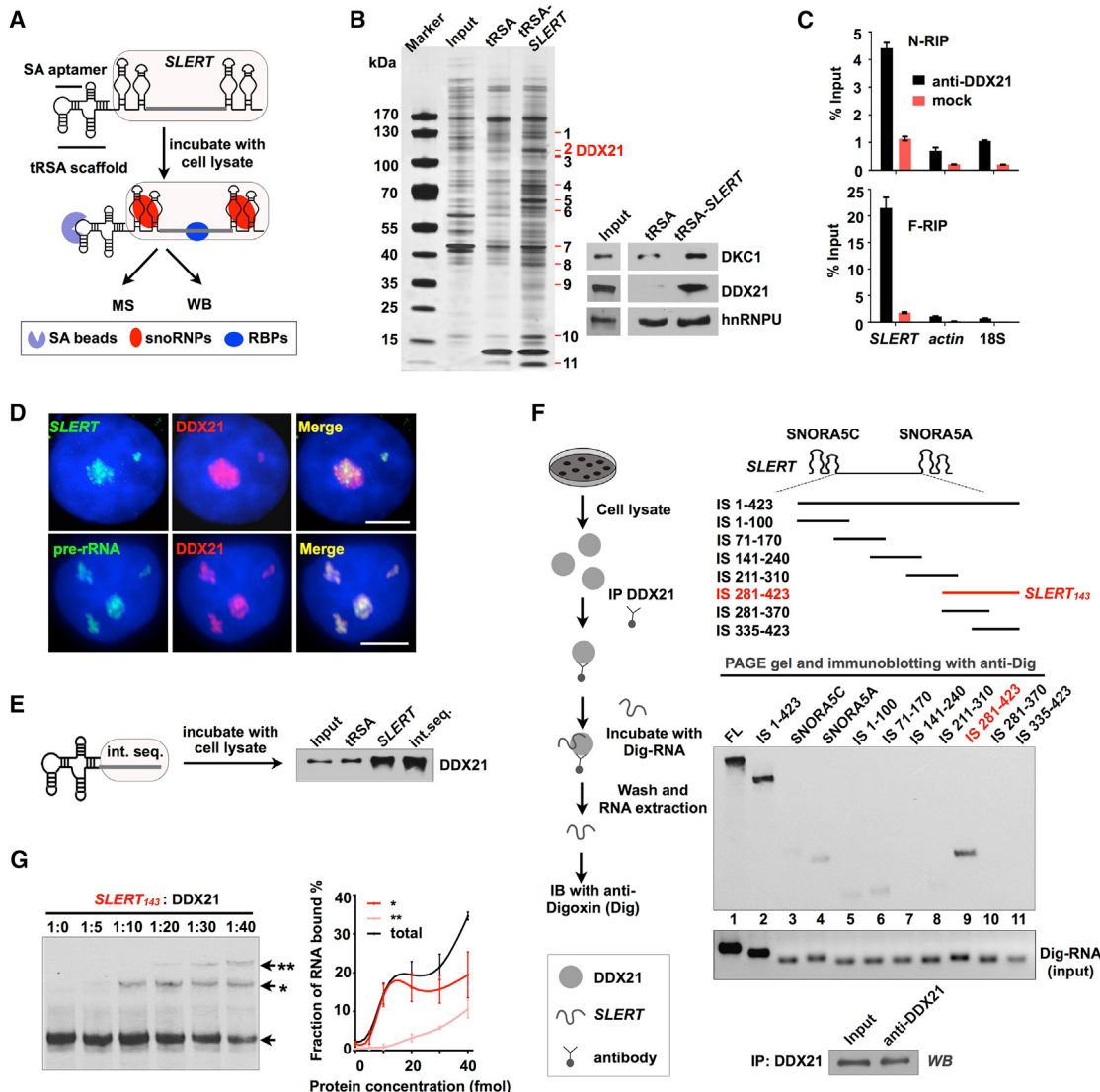


**Figure 3. SLERT Interacts with the DEAD-Box RNA Helicase DDX21 in the Nucleolus**

(A) Schematic drawing of the tRSA RNA pull-down assay.

(B) Identification of proteins associated with *SLERT*. Left: silver staining of tRSA pull-down proteins; tRSA-SLERT-enriched bands were analyzed by MS. Right: WB-validated *SLERT*-interacting proteins. The irrelevant lanes were digitally eliminated from the blot image. See also Figures S2A–S2C.

(C) Native (upper panel) or formaldehyde cross-linking (lower panel) RIP of DDX21 in PA1 cells using anti-DDX21 or anti-IgG antibodies. The percentage of RIP-enriched RNA relative to input was calculated by qRT-PCR. Error bars represent SD in triplicate experiments.

(D) Co-localization of *SLERT* and DDX21 in the nucleolus. Co-staining of *SLERT* (green) and DDX21 (red) or pre-rRNA (green) and DDX21 (red) in PA1 cells. Scale bar, 5 μm.

(E) tRSA pull-down of full-length and non-snoRNA internal sequence of *SLERT*.

(F) Partially purified DDX21 interacts with the 3' domain of *SLERT* internal sequence. Left: schematic drawing of the experimental flow. Right: in vitro binding assays between DDX21 and Dig-labeled *SLERT* fragments identified a 143-nt non-snoRNA sequence for the interaction. Right bottom: WB revealed the DDX21 pull-down efficiency.

(G) *SLERT*<sub>143</sub> interacts with DDX21. Left: EMSA image of the Dig-labeled *SLERT*<sub>143</sub> binding to varying concentrations (starting from 5 fmol) of purified DDX21. One and two asterisks denote monomer and dimer status, respectively, and the arrow without any asterisk indicates RNA-only. Right: quantitation of EMSA images; error bars within binding curves represent three independent experiments, performed on different days. See also Figure S2D.

RPA194 in PA1 (Figure 4F; Movie S3) and HeLa (Figure S3G) cells. Moreover, the same localization between DDX21 and another subunit of the Pol I complex, RPA49, was found in PA1 (Figure 4G) and HeLa (Figure S3H) cells. Finally, similar observa-

tions were observed in examined HEK293 and SH-SY5Y cell lines (Figure S3I).

The remarkable DDX21 and Pol I arrangement suggests that DDX21 plays an important role in Pol I transcription. In

agreement with their localization (Figures 4 and S3), DDX21 chromatin immunoprecipitation (ChIP) revealed that DDX21 bound to promoter and 28S/18S regions, but not to intergenic spacer (IGS) sequence of rDNA clusters (Figure S3J). Similar ChIP results were also reported (Calo et al., 2015). Further co-immunoprecipitation (coIP) showed the interaction between DDX21 and RPA194 (Figure 4H). Knockdown of DDX21 in PA1 cells by two different short hairpin RNAs (shRNAs) (Figure 4I) led to both increased steady-state (Figure 4J) and nascent (Figure 4K) levels of 47S pre-rRNA. Meanwhile, we observed increased Pol I engagements to the promoter and 28S/18S regions, but not to IGS sequences of rDNA clusters (Figure 4L), indicating that DDX21 suppresses rDNA transcription by preventing Pol I loading to rDNAs. Together, these results suggest that the DDX21 ring-like structures are associated with suppressed pre-rRNA transcription.

#### DDX21 Ring Structures Assemble at the Border between FC and DFC and Their Sizes Correlate with Pre-rRNA Production

The nucleolus can be divided into three subregions, fibrillar center (FC), dense fibrillar component (DFC), and granular compartment (GC). Transcription of rDNA repeats occurs mainly at the border between FC and DFC with Pol I subunits being enriched in the FC region. The processing and modification of pre-rRNA transcripts occurs largely in DFC where the snoRNPs accumulate (Boisvert et al., 2007). Co-localization studies revealed that DDX21 largely overlapped with the DFC marker fibrillarin, but not the GC marker B23 (Figures S4A and S4B). Together with the observation that DDX21 rings coat Pol I complexes (Figures 4 and S4C), all findings support the view that DDX21 rings are assembled at the border between FC and DFC, where the transcription of rDNA repeats occurs in active NORs. Further co-localization studies among DDX21, RPA194, and rDNAs showed that rDNAs were engaged to multiple Pol I complexes surrounded by individual DDX21 rings (Figures 5A and S4D). Of note, the ring structures were somewhat impaired by the harsh denatured condition during FISH procedure. Also, we found that not all rDNAs were co-localized with DDX21 (Figure S4E), further indicating that DDX21 rings only associate with actively transcribed NORs (Figures 4D–4G and 5A).

The transcription-dependent ring-shaped structures surrounding Pol I complexes (Figure 4) and their specific subnuclear localization (Figures 5A and S4A–S4D) let us ask how DDX21 rings affected pre-rRNA synthesis at active NORs. We used RNA FISH, with a probe recognizing 47S pre-rRNA, to examine pre-rRNA produced from each DDX21 ring by measuring the relative pre-rRNA fluorescence intensity that coats the ring (Figure S5A). Strikingly, all detectable DDX21 ring-like structures were coated by pre-rRNAs, and all detectable pre-rRNAs were associated with the ring structures (Figure 5B). The fluorescence intensity of pre-rRNA coated on an individual DDX21 ring was positively correlated with the diameter of each corresponding ring structure (Figure 5C), indicating that the enlarged DDX21 rings are correlated with augmented pre-rRNA transcription, although DDX21 rings alone act to suppress Pol I transcription (Figures 4H–4L).

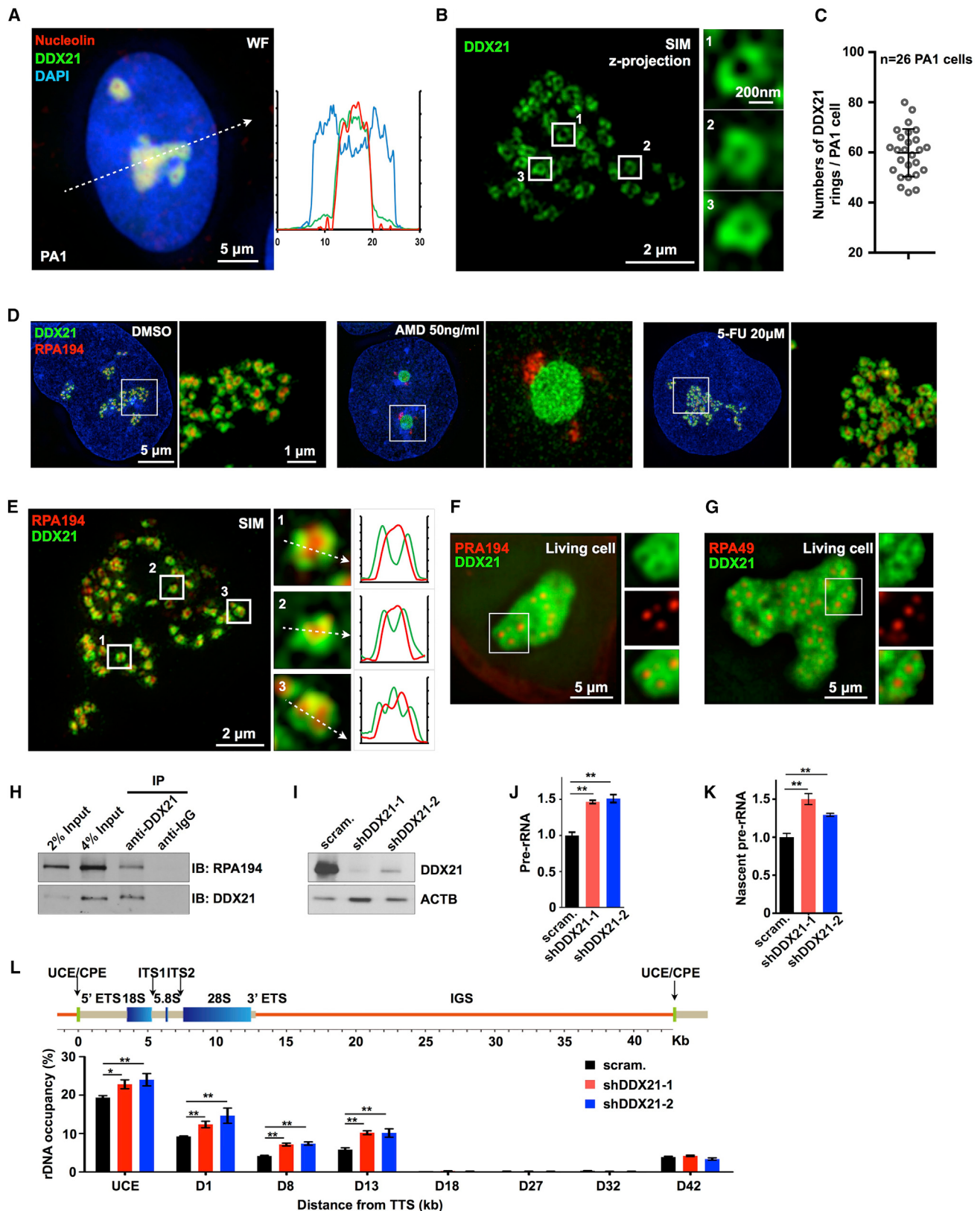
#### **SLERT Binds and Modulates DDX21 Rings by Allosterically Changing Individual DDX21 Molecules**

The next question was what factors could regulate DDX21 rings to promote Pol I transcription? Because *SLERT* enhances Pol I transcription (Figure 2) and interacts with DDX21 (Figure 3), we then examined the spatial localization of *SLERT*, DDX21, and Pol I under SIM. Co-visualization among these three factors revealed that *SLERT* was located to DDX21 rings, but not Pol I (Figure 5D). We observed that one to several *SLERT* spots were specifically co-localized to DDX21 rings (Figure 5E), but almost no-colocalization between *SLERT* and Pol I was found. These observations strongly suggest that *SLERT* enhances Pol I transcription via DDX21 rings.

How do DDX21 and *SLERT* act together to carry out their distinct roles in rRNA biogenesis? One possibility was that depletion of *SLERT* might reduce DDX21 expression, which in turn inhibited Pol I transcription (Figures 4H–4L). However, expression of both DDX21 and RPA194 was not altered in *SLERT* KO, excluding this gene expression regulatory loop model (Figure S4F).

Another possibility was that *SLERT* could alter the conformation of DDX21 rings coating Pol I complexes, resulting in enhanced pre-rRNA production. SIM observations of DDX21 and RPA194 in PA1 cells that were depleted or overexpressed *SLERT* indeed showed remarkable differences regarding the size of DDX21 rings (Figures 5F, top panel, and S6). *SLERT* KO consistently reduced DDX21 ring sizes, with diameters from an average of ~395 nm ( $394.8 \pm 84.59$  nm) in wild-type PA1 cells to an average of ~360 nm in two *SLERT* KO cell lines (KO-1,  $364.4 \pm 76.75$  nm; KO-2,  $357.8 \pm 75.69$  nm) (Figures 5F and S6A–S6C), whereas OE *SLERT* in *SLERT* KO cell lines could not only rescue but also enlarge DDX21 rings to ~420 nm compared to those in wild-type cells (KO-1 + *SLERT* OE,  $423.6 \pm 99.26$  nm; KO-2 + *SLERT* OE,  $417.8 \pm 90.76$  nm; WT + *SLERT* OE,  $413.6 \pm 90.3$  nm; Figures 5F and S6D–S6F). Of note, the abundance of overexpressed *SLERT* is ~25- to 40-fold of its endogenous level in wild-type cells (Figure 5F, middle panel). Correspondingly, pre-rRNA production was also reduced or increased in *SLERT* KO or OE cells (Figure 5F, bottom panel).

We then examined the localization pattern between *SLERT* and DDX21 rings in *SLERT* OE cells. We expected to see a more evenly distributed *SLERT* overlapping with individual rings because its copy numbers were significantly increased from ~156 (Figure S1A) to 4,000–6,000 (Figure 5F) per cell in the nucleolus. Surprisingly, however, we observed a similar pattern between *SLERT* and these ring-shaped arrangements in *SLERT* OE and WT cells (Figures 5E and S4G): only one to several *SLERT* spots were specifically co-localized to DDX21 rings (Figure 5E). This observation suggests that *SLERT* does not randomly interact with the ring but prefers to bind specific places of each ring-like structure. Remarkably, although the co-localization pattern between *SLERT* and DDX21 rings remained unchanged, the fluorescence intensity of *SLERT* coating per ring was increased in *SLERT* OE cells (Figure 5G). Further analyzing *SLERT* integrated fluorescence intensities associated with individual DDX21 rings and the ring's diameter revealed their positive correlation in a power function distribution (Figures 5G and S5B). Thus, although *SLERT* positively controls the size of



(legend on next page)

DDX21 ring-shaped structures within a certain range, the rings cannot reach unlimited size for Pol I transcription regulation no matter how many additional *SLERT* lncRNAs are introduced into cells. These results indicate a tight regulation of DDX21 rings on Pol I transcription.

The conformational change of DDX21 rings regulated by *SLERT* (Figure 5) led us to speculate that binding by *SLERT* would allosterically change individual DDX21 molecules, which could occur where *SLERT* binds within each ring. To test this hypothesis, we developed a Förster resonance energy transfer (FRET) assay to examine the conformational change of individual DDX21 molecules in the presence and absence of *SLERT*. We fused EGFP to the N-terminal end of DDX21 and mCherry to the C-terminal end of DDX21 (EGFP-DDX21-mCherry). FRET would occur only when N- and C-terminal domains of DDX21 were in close proximity (<10 nm) (Figure 6A, left panel). We found that the FRET efficiency of EGFP-DDX21-mCherry in each of two *SLERT* KO cells was consistently decreased compared to that in normal cells (Figure 6A, right panel), suggesting that more “open” conformational change between N- and C-terminals of DDX21 could occur in the absence of *SLERT* (Figure 6A). As controls, no change of inter-molecular interaction between C-terminal mCherry-fused DDX21 and N-terminal EGFP-fused DDX21 could be detected by FRET in wild-type or *SLERT* KO cells (Figure 6B).

#### Modulation of DDX21 by *SLERT* Alters Its Binding to Pol I and the Pol I Occupancy at rDNAs

To investigate the effect of *SLERT* binding on DDX21, we mapped how DDX21 interacted with *SLERT* and Pol I in the nucleolus. DDX21 has N- and C-terminal domains and two conserved RecA domains (D1 and D2 for short) involved in ATP binding and hydrolysis (Bourgeois et al., 2016). Application of NoD, a web server that has been used to predict nucleolar localization sequence (NoLS) (Scott et al., 2011), revealed that DDX21 contains NoLSs located in its N- and C-terminal domains (Figure S7A). This was further confirmed by the observation that DDX21 lacking the N- or the C-terminal domain was no longer localized to the nucleolus, and DDX21 lacking the D1 or the D2

domain was still enriched in the nucleolus (Figure S7B). We next generated a series of DDX21 truncations carrying both N- and C-terminal NoLSs to ensure all expressed DDX21 mutants were located in the nucleolus (Figure S7C). PA1 cells transfected with individual Flag-tagged DDX21 truncations (Figure 6C) were precipitated by anti-Flag antibodies, followed by the detection of each Flag-DDX21-truncation-associated RPA194 (Figure 6D, upper panels) or by incubation with *SLERT* in vitro (Figure 6D, bottom panels). We found that Pol I interacted with DDX21 mainly via one RecA domain and its C-terminal domain (Figure 6D, lanes 1 and 6). While *SLERT* interacted with both RecA domains of DDX21, the interaction was stronger in the presence of both RecA domains (Figure 6D, lanes 1–3) and it barely bound to the N- or C-terminal domains (Figure 6D, lanes 4–6). Thus, DDX21 interacts with *SLERT* and Pol I via distinct but partially overlapping domains.

Because RecA domains of DDX21 are required for RNA helicase activity (Bourgeois et al., 2016) and these two domains are associated with *SLERT*, we asked whether the helicase activity would have an effect on pre-rRNA production. DDX21 was knocked down by shRNAs (Figure 4I) that target its 3' UTR, followed by introduction of either wide-type DDX21 or the helicase null (Perlaky et al., 1997) DDX21<sup>DEV</sup> (DEVD to HGVD) or DDX21<sup>SAT</sup> (SAT to LET) mutants into DDX21 KD cells. Consistent with Figure 4I, the level of pre-rRNA was increased after DDX21 KD in PA1 cells, and importantly, this effect could be rescued by both wild-type and two mutants of DDX21 lacking helicase activity (Figures S7D and S7E), suggesting that Pol I transcription regulation by DDX21 is unlikely to be associated with its helicase activity.

The distinct binding capability of different domains of DDX21 with *SLERT* and Pol I let us ask whether the allosterically altered DDX21 upon *SLERT* depletion could result in altered binding capability to Pol I. CoIP experiments revealed that interaction between DDX21 and RPA194 increased to ~3-fold in cells lacking *SLERT* (Figure 6E), indicating that the “open” DDX21 in the absence of *SLERT* enhances its interaction with Pol I (Figures 6A and 6E). In vitro competition assays carried out with purified His-DDX21 (Figure S2D), GST-RPA194 (Figure S7F), and *SLERT*

**Figure 4. DDX21 Forms Ring-like Structures Surrounding the Pol I Complexes in the Nucleolus**

- (A) DDX21 accumulates in the nucleolus. A representative image shows the co-staining of DDX21 (green) and nucleolin (red). Right: plot profile of the image.
- (B) DDX21 forms ring-shaped structures in the nucleolus in PA1 cells revealed by SIM with anti-DDX21 antibodies. Right panels: three DDX21 rings in single z section. See also Figures S3A–S3D and S3I and Movies S1 and S2.
- (C) Statistics of the number of DDX21 rings detected per PA1 cell. Data are expressed as mean  $\pm$  SD.
- (D) DDX21 rings are disrupted by Pol I transcription inhibition. Images of DDX21 (green) and RPA194 (red) by SIM in PA1 cells pretreated with AMD or 5-FU for 3 hr with indicated concentrations were shown. See also Figures S3E and S3F.
- (E) The Pol I complexes are located within DDX21 rings. Left: co-staining of DDX21 (green) and RPA194 (red) by SIM in PA1 cells. Right: plot profiles of representative images of DDX21 rings and RPA194.
- (F) RPA194 is surrounded by DDX21 rings in live PA1 cells. DDX21-mCherry (green) and EGFP-RPA194 (red) are shown in pseudocolor. See also Figure S3G and Movie S3.
- (G) RPA49 is surrounded by DDX21 rings in live PA1 cells. DDX21-mCherry (green) and EGFP-RPA49 (red) is shown in pseudocolor. See also Figure S3H.
- (H) DDX21 interacts with RPA194 in PA1 cells. See also Figure S3J.
- (I) DDX21 KD by two different shRNAs, revealed by WB.
- (J and K) Pre-rRNA transcription is suppressed by DDX21. DDX21 KD led to enhanced steady-state (J) and nascent (K) levels of pre-rRNAs, normalized to actin mRNA. Error bars represent SD in triplicate experiments. \*p < 0.05 and \*\*p < 0.01 (Student's t test).
- (L) DDX21 KD enhanced RPA194 occupancy at rDNAs. Top: a schematic drawing of one rDNA cluster. Bottom: ChIP-qPCR of the RPA194 genomic occupancy at rDNAs in scramble or two DDX21 KD cell lines. UCE, upstream control element. “D’s” represent distances from the transcription start site to specific primer sets located in a 43-kb rDNA repeat. Error bars represent SD in triplicate experiments. \*p < 0.05 and \*\*p < 0.01 (Student's t test).

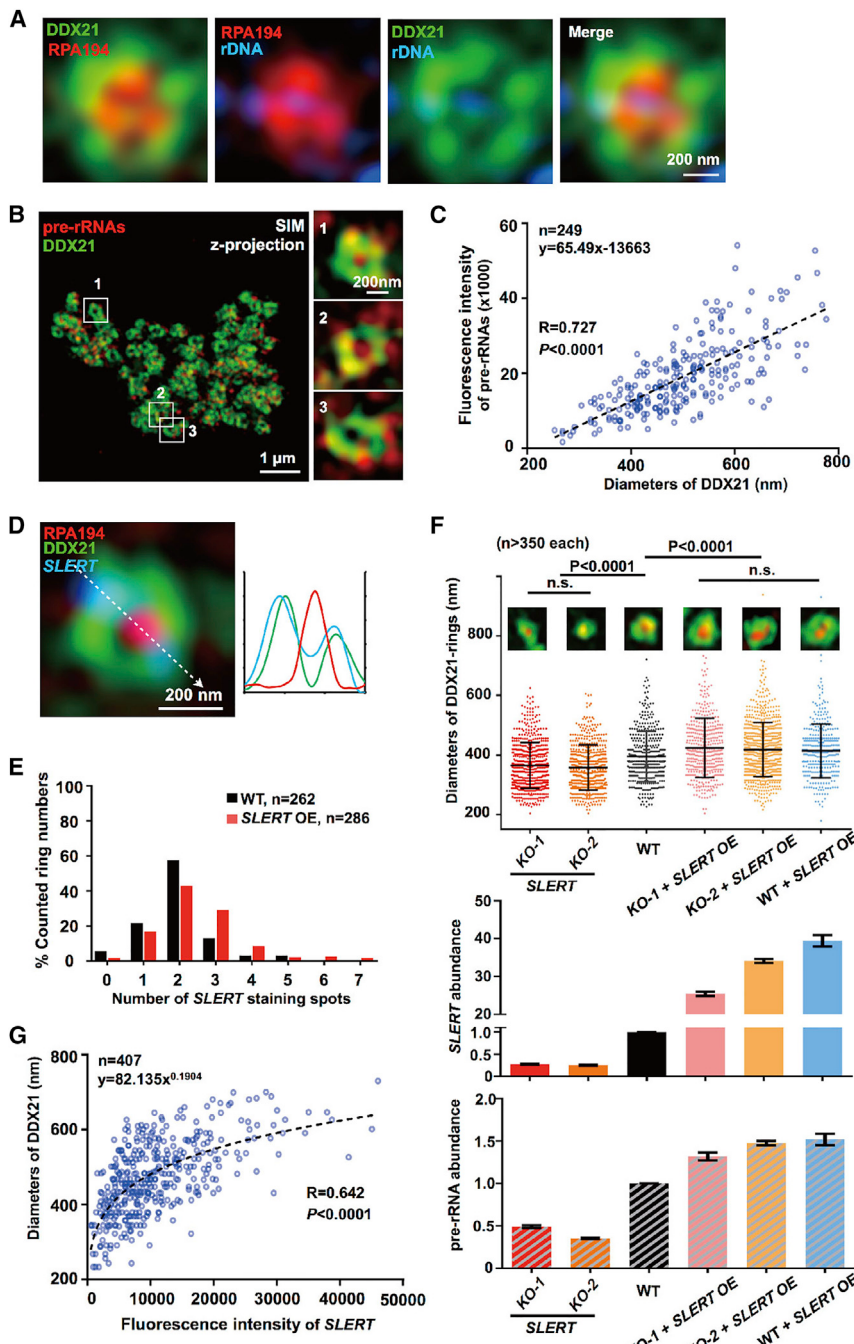


**Figure 5. SLERT Controls the Sizes of DDX21 Ring-Shaped Structures**

(A) rDNA repeats are engaged to Pol I complexes surrounded by DDX21 rings. A representative image of co-staining DDX21 (green), RPA194 (red), and rDNAs (blue) by SIM in PA1 cells was shown (see also Figures S4A–S4E). rDNA repeats were detected by DNA FISH with a probe recognizing the rDNA repeat unit shown in Figure S4D.

(B) Pre-rRNAs coat individual DDX21 ring-shaped arrangements. A representative image of co-staining DDX21 (green) and pre-rRNAs (red) by SIM and three rings in single z section in PA1 cells is shown. Pre-rRNAs were detected by FISH with a probe shown in Figure 2D.

(C) The production of pre-rRNAs is positively correlated with the size of DDX21 rings. The integrated fluorescence intensity of pre-rRNAs coating each ring and the diameter of corresponding 249 DDX21 rings from 13 PA1 cells in two replicates were measured and plotted. See also Figure S5A.

(D) SLERT interacts with DDX21 rings but not Pol I complexes.

A representative image of co-staining DDX21 (green), RPA194 (red), and SLERT (blue) by SIM and a plot profile of the image are shown.

(E) Co-localization between SLERT and DDX21 rings. DDX21 rings from 16 wild-type or SLERT OE PA1 cells were collected by SIM and the number of SLERT spots in each ring were counted. See also Figure S4G.

(F) The positive correlation of SLERT expression, DDX21 ring size, and pre-rRNA production. Co-staining of DDX21 (green) and RPA194 (red) by SIM in SLERT KO, wild-type, and SLERT OE in either SLERT KO or wild-type PA1 cells. Top: single layer image of representative DDX21 ring under SIM and the statistics of DDX21 ring size under each condition (Mann-Whitney test). Of note, the longest distance was set as the length of diameter of each ring. Data are expressed as mean  $\pm$  SD. Middle: SLERT expression of each examined condition as revealed by qRT-PCR. Bottom: pre-rRNA production of each examined condition as revealed by qRT-PCR, normalized to actin. See also Figure S6. Error bars represent SD in triplicate experiments in middle and bottom panels.

(G) The amount of SLERT binding to DDX21 ring and the corresponding size of ring shows a power function distribution. The integrated fluorescence intensity of SLERT overlapping with each DDX21 ring and the diameter of corresponding 407 DDX21 rings from 19 SLERT OE PA1 cells in three replicates were measured and plotted. See also Figure S5B.

revealed a direct interaction between DDX21 and RPA194 (Figure 6F, lane 3); remarkably, such direct interaction could be almost completely interrupted by the addition of SLERT (Figure 6F, lanes 4 and 5) but not the control egfp RNA (Figure 6F, lanes 6 and 7), confirming that SLERT specifically binding to DDX21 (Figure 3) impairs the interaction between DDX21 and Pol I.

Importantly, we observed a consistent increase of RPA194 occupancy to the promoter and 28S/18S regions of rDNAs in cell

lines overexpressing WT-SLERT, but not egfp-SLERT (Figure 6G), and a consistent decrease of RPA194 occupancy to rDNAs in SLERT KO cell lines (Figure 6H). These observations suggest that a stronger interaction between DDX21 and Pol I (Figures 6E and 6F) can redirect Pol I complexes away from rDNAs in the absence of SLERT, consistent with the observation that knockdown of DDX21 to remove the suppression on Pol I led to increased Pol I occupancies to rDNA clusters (Figure 4L). Together, these results support a model where depletion of

*SLERT* allosterically alters individual DDX21 molecules leading to enhanced interaction between DDX21 and Pol I, tightened DDX21 rings surrounding Pol I complexes, and subsequent suppression of rDNA transcription by Pol I (Figure 7A).

### SLERT Promotes Tumorigenesis

It is well-established that dysregulated rRNA synthesis by Pol I is associated with uncontrolled cancer cell proliferation, and Pol I is a potential therapeutic target (Nguyen et al., 2015; Peltonen et al., 2014). The observation that *SLERT* augmented Pol I transcription via DDX21 (Figure 7A) led us to examine whether altered *SLERT* levels would affect cell proliferation. Colony formation assays revealed that the loss of *SLERT* impaired cell growth (Figure 7B). Furthermore, mice with xenografts of *SLERT* KO cells developed smaller tumor mass than those of control cells (Figure 7C). Moreover, OE of *WT-SLERT*, but not *egfp-SLERT*, promoted colony formation (Figure 7D) and cell proliferation (Figure 7E), excluding a potential role of box H/ACA snoRNAs in tumorigenesis. These experiments strongly argue that a high level of *SLERT* in cells is biologically relevant in tumorigenesis, and the interaction between *SLERT* and DDX21 represents a potential therapeutic target for future anti-cancer drug discovery.

### DISCUSSION

rDNA is the most highly transcribed region of the eukaryotic genome and more than 60% of total cellular transcription results from Pol I activity (Warner, 1999). The Pol I complex contains 14 subunits in eukaryotes, and a number of factors are known to regulate Pol I transcription, with most of them acting at the initiation stage by promoting Pol I activity (Boisvert et al., 2007; Goodfellow and Zomerdijk, 2013; Nguyen et al., 2015; Schneider, 2012). In order to achieve a balance between cellular growth requirements and rRNA production, Pol I transcription needs to be precisely monitored and calibrated in cells. However, few suppressors of Pol I transcription have been reported. Here, we report two previously unknown factors, *SLERT* and DDX21, that work together to regulate Pol I transcription. DDX21 forms ring-shaped arrangements surrounding multiple Pol I complexes, and *SLERT* is a key regulatory RNA that remodels the clamp of DDX21 rings acting on Pol I (Figure 7A).

DDX21, also named RNA helicase II or Gu ( $\alpha$ ) protein, was first identified from nuclear extracts of HeLa cells (Flores-Rozas and Hurwitz, 1993). It has RNA unwinding activity (Perlaky et al., 1997; Valdez et al., 1996) and is involved in pre-rRNA processing (Henning et al., 2003; Holmström et al., 2008; Sloan et al., 2015). Calo et al. (2015) have recently reported that DDX21 associates with Pol I and Pol II transcribed genes to coordinate transcription and rRNA processing. They have shown that DDX21 binds to 7SK RNA and is recruited to the promoters of Pol II-transcribed genes encoding ribosomal proteins and snoRNAs to enhance transcription in the nucleoplasm. It was also suggested that DDX21 could promote rRNA transcription, processing, and modification in the nucleolus, however, no clearly defined mechanism of action of nucleolar DDX21 was shown.

Here, we demonstrate that DDX21 molecules in the nucleolus form ring-shaped structures that are coupled to Pol I transcription (Figure 4). While DDX21 rings alone suppress pre-rRNA tran-

scription, enlarged DDX21 rings upon *SLERT* binding can overcome such repression, leading to augmented pre-rRNA production (Figures 4 and 5). At the molecular level, binding by *SLERT* alters individual DDX21 protein conformation, reduces their interaction with Pol I subunits, and liberates Pol I to transcribe rDNAs more actively (Figure 6). Although each ring is only coated by two to three *SLERT* lncRNAs (Figures 4C, 5D, 5E, S1A, and S4G), one *SLERT* is able to bind to multiple DDX21 molecules (Figure 3G) at preferred places on individual rings (Figures 5D and 5E). Thus, it is attractive to speculate that the *SLERT-DDX21*-regulated Pol I transcription occurs at where *SLERT* binds in individual rings, and such regional changes can affect DDX21 and Pol I interaction, and subsequently, the extent of Pol I occupancies to transcribed rDNA clusters (Figures 6 and 7A). Consistently, we observed that *SLERT* depletion led to a dramatic reduction of pre-rRNA transcription (Figure 2). Of note, the level of *SLERT* expression, which is ~200 copies per cell (Figure S1A), is much less abundant than that of other core components of the Pol I machinery. So, how is the level of *SLERT* expression reconciled to the extent of its impact on Pol I transcription? Indeed, *SLERT* copy number per cell is comparable to the number of active rDNA genes per cell, as only a fraction of the 400 rDNA genes remain transcriptionally active in any cell type (Boisvert et al., 2007). Together, these findings represent an important mechanism in controlling the differential expression of rDNA genes within a specific NOR cluster (Figure 7A). The proposed regulation can be prevalent, supported by the observation that all detectable Pol I complexes in examined human cells are surrounded by DDX21 rings and *SLERT* (Figures 4, S3, and S6).

We do not yet know how many DDX21 molecules are required to form one DDX21 ring around multiple Pol I complexes. Using SIM and stoichiometric quantity of whole cellular extracts plotting with purified DDX21, each DDX21 ring-shaped arrangement was estimated to contain several to over 10,000 molecules. However, as the three-dimensional arrangement of DDX21 rings and the exact assembly pattern between DDX21 molecules within each structure require improved techniques to elucidate, this number is only speculative. Nevertheless, this stoichiometric outcome raises an intriguing question: how do two to three *SLERT* molecules, although each binds to multiple DDX21 proteins, change conformation of the ring that contains thousands of copies of DDX21 proteins? Our data support one possibility that binding *SLERT* to DDX21 is sufficient to elicit regionally allosterical alteration, which in turn may lead to the observed change of the ring-shaped arrangements (Figures 5 and 6). In addition, DDX21 rings may act beyond Pol I transcription regulation. For instance, DDX21 was reported to be involved in pre-rRNA processing and modification (Calo et al., 2015; Henning et al., 2003; Sloan et al., 2015); it is likely that the formation of DDX21 rings may coordinate pre-rRNA transcription and modification to achieve a higher pre-rRNA processing efficiency. Understanding both biochemical and structural details of the DDX21 ring, the *SLERT-DDX21* complex, and interaction with Pol I complexes will be necessary to fully understand this complex regulation.

*SLERT* is human-specific (Zhang et al., 2014). One of the two snoRNAs at its ends, SNORA5A, is only present in human but not

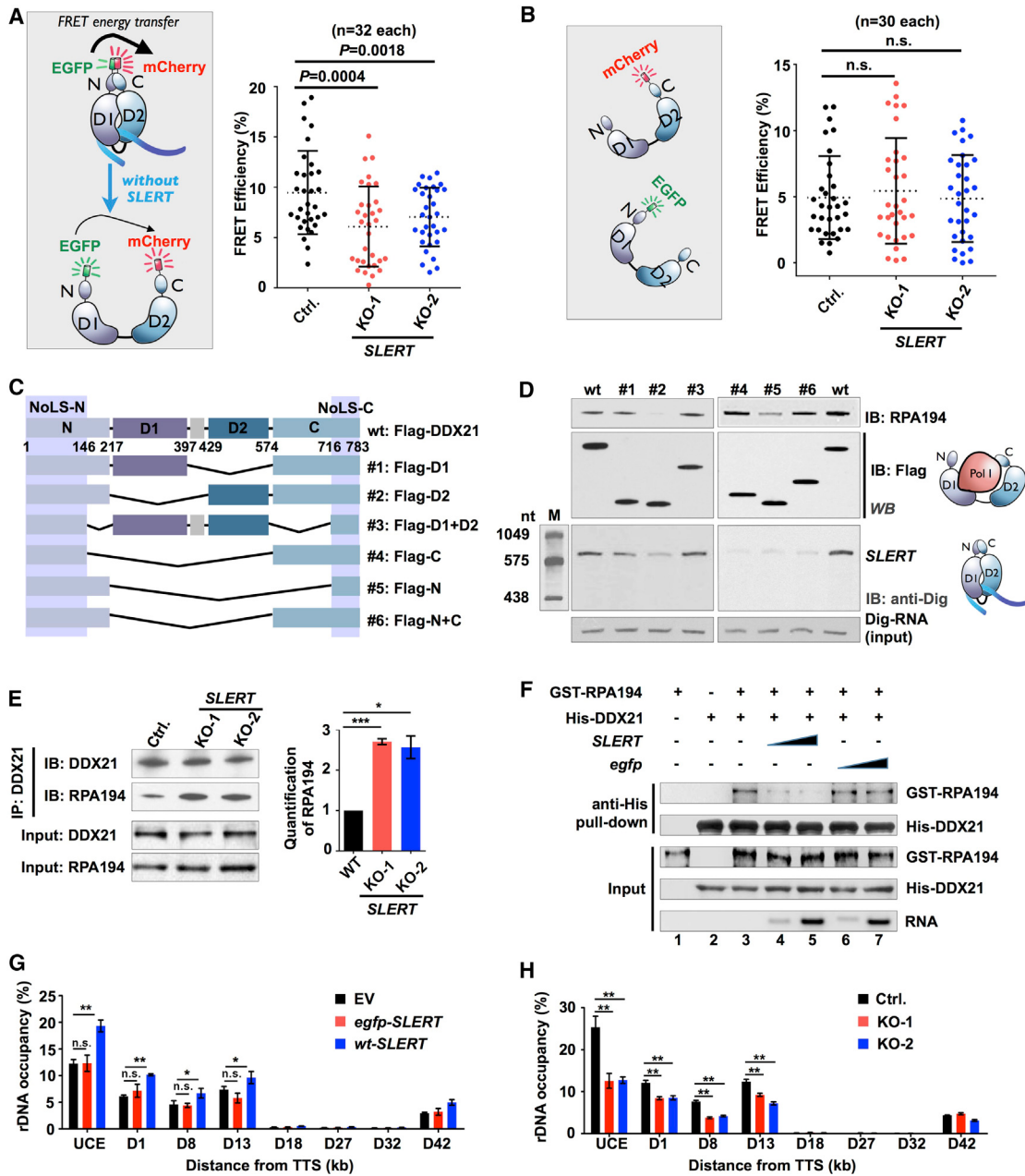


**Figure 6. Modulation of DDX21 by SLERT Alters Its Binding to Pol I and the Pol I Occupancy at rDNAs**

(A) Binding of SLERT induces intra-molecular conformational change of individual DDX21 molecules. Left: schematic drawing to show the conformational change of DDX21 with or without SLERT. Right: FRET efficiencies between EGFP (N) and mCherry (C) of EGFP-DDX21-mCherry in control and SLERT KO cells were measured and plotted (Student's t test).

(B) Binding of SLERT does not induce inter-molecular interaction of DDX21. Left: schematic drawing to show two DDX21 molecules that either fused EGFP as a donor at the N-terminal or mCherry as an acceptor at the C-terminal. Right: FRET efficiencies between EGFP-DDX21 and mCherry-DDX21 in control and SLERT KO cells.

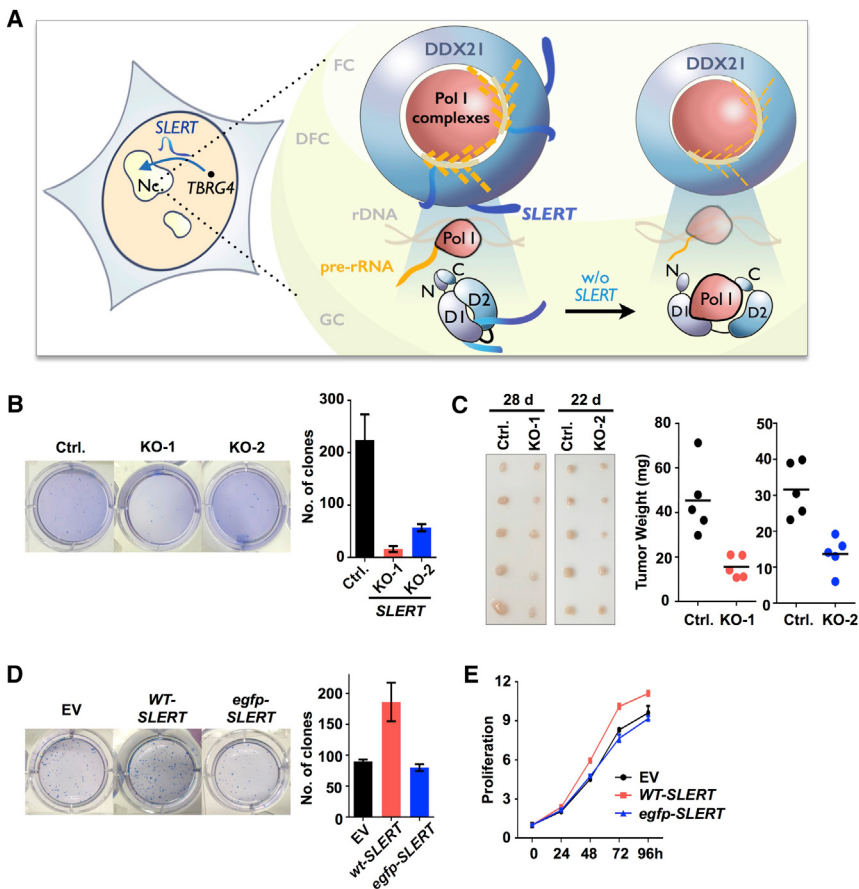
(C) Schematic drawing of DDX21 truncations used in (D). Each truncated DDX21 contains NoLS at its N-terminal and C-terminal. The black lines represent deleted regions in DDX21 truncations.

(D) DDX21 binds to RPA194 and SLERT via distinct but overlapping domains. Top: coIP of truncated DDX21 shown in (C) and RPA194 with anti-Flag antibodies. Bottom: Dig-labeled RNA pull-down of the truncated DDX21 (see Figure 3F for details). See also Figures S7A–S7C.

(E) SLERT depletion leads to increased interaction between DDX21 and RPA194, revealed by coIP of DDX21 and RPA194 in control and SLERT KO PA1 cells. The relative ratio of RPA194 and DDX21 from no less than three independent experiments was determined using Quantity One software and is shown on the right.

(F) SLERT impairs the binding between GST-RPA194 and His-DDX21. Purified GST-RPA194 (10 pmol) and His-DDX21 (10 pmol) were incubated in vitro in the presence or absence of SLERT or EGFP control RNA (10 pmol and 50 pmol), followed by anti-His pull-down and WB (see also Figure S7F). Representative results are shown from three replicates.

(legend continued on next page)

**Figure 7. SLERT Promotes Tumorigenesis**

(A) Proposed model for *SLERT* and *DDX21* in Pol I transcription regulation. See text for details.

(B) The colony formation assay in *SLERT* KO cells. Error bars represent SD in triplicate experiments.

\*\* $p < 0.01$  (Student's t test).

(C) Xenograft assay of *SLERT* KO cells in nude mouse.

(D) The colony formation assay in control, *WT-SLERT*, and *egfp-SLERT* OE PA1 cells. Error bars represent SD in triplicate experiments. \*\* $p < 0.01$  (Student's t test).

(E) The proliferation assay in control, *WT-SLERT*, and *egfp-SLERT* OE PA1 cells. Error bars represent SD in triplicate experiments. \*\* $p < 0.01$  (Student's t test).

in mouse. Thus, no *SLERT* could be produced from introns of mouse *TBRG4*. It will be of interest to examine whether *DDX21* forms similar rings in mouse cells and whether similar regulatory RNAs exist for Pol I regulation. Of note, the Pol I machinery is dedicated solely to transcribing rDNAs and is rapidly evolving, which can be exemplified by incompatibilities between mouse and human (McStay, 2006, 2016). Interestingly, human *SNORA5A* was predicted as a guide RNA of pseudouridylation for residues 1242 and 1629 of 18S rRNA (Kiss et al., 2004), while no such modifications were reported in mouse.

Dysregulated rRNA synthesis by Pol I is associated with cancer cell proliferation. Thus, targeting the Pol I activity could offer a therapeutic opportunity (Peltonen et al., 2014). Modulation of *SLERT* expression led to impaired or promoted cell proliferation (Figure 7). While directly blocking Pol I transcription may cause non-specificity in potential anti-cancer drug discovery, targeting *SLERT* or the interaction between *SLERT* and *DDX21* represent potential therapeutic targets for anti-cancer. In sum, our findings uncover a fundamental control of ribosome biogenesis in human

cells by altering *SLERT* expression, changing *DDX21* conformation, and modulating *DDX21* ring-shaped structures that act on Pol I transcription.

## STAR METHODS

Detailed methods are provided in the online version of this paper and include the following:

- KEY RESOURCES TABLE
- CONTACT FOR REAGENT AND RESOURCE SHARING
- EXPERIMENTAL MODEL AND SUBJECT DETAILS
  - Human Cell Lines
  - Subcutaneous Xenograft Tumor Models
- METHOD DETAILS
  - Plasmids Construction
  - Cell Culture, Cell Transfection and Lentiviral Infection
  - Protein Expression and Purification
  - Isolation of Nucleoli

(G) *WT-SLERT* OE, but not *egfp-SLERT*, leads to enhanced RPA194 occupancy at rDNAs revealed by ChIP of the RPA194 occupancy at rDNAs in indicated cell lines. See Figure 4L for details.

(H) *SLERT* KO reduces RPA194 occupancy at rDNAs revealed by ChIP of the RPA194 occupancy at rDNAs in control or *SLERT* KO cells.

In (A) and (B), data are expressed as mean  $\pm$  SD. In (E), (G), and (H), error bars represent SD in triplicate experiments. \* $p < 0.05$ , \*\* $p < 0.01$ , \*\*\* $p < 0.001$  (Student's t test).

- RNA Isolation, qRT-PCR and Northern Blotting
- Measurement of *SLERT* Copy Numbers
- RNA In Situ Hybridization and Immunofluorescence Microscopy
- RNA/DNA Double FISH
- Structured Illumination Microscopy Procedure
- Structured Illumination Microscopy Imaging Analysis
- Live Cell Imaging
- Knockout *SLERT* by CRISPR/CAS9
- Collection and Quantification of Nascent pre-rRNA
- Dual Luciferase Reporter Assay
- Ribosome Fractionation
- tRNA Pull-down Assay and Western Blotting
- Silver Staining and Mass Spectrometry
- Native RNA-Protein Complex Immunoprecipitation
- Formaldehyde Crosslinking RNA Immunoprecipitation
- Co-Immunoprecipitation
- In vitro Competition Binding Assay
- Dig-Labeled RNA Pull-down Assay
- Electrophoretic Mobility Shift Assay
- Förster Resonance Energy Transfer Assay
- Chromatin Immunoprecipitation
- Soft Agar Colony Formation Assay
- Cell Proliferation Assay

## ● QUANTIFICATION AND STATISTICAL ANALYSIS

### SUPPLEMENTAL INFORMATION

Supplemental Information includes seven figures, one table, and three movies and can be found with this article online at <http://dx.doi.org/10.1016/j.cell.2017.04.011>.

### AUTHOR CONTRIBUTIONS

Conceptualization, L.-L.C.; Methodology, Y.-H.X., R.-W.Y., Y.Z., and L.-L.C.; Software, Y.-H.X., R.-W.Y., R.D., and L.Y.; Validation, Y.-H.X., R.-W.Y., and Y.Z.; Investigation, Y.-H.X., R.-W.Y., Y.Z., C.-J.G., S.J., and G.X.; Data Curation, Y.-H.X., R.-W.Y., Y.Z., C.-J.G., and L.-L.C.; Writing – Original Draft, Y.-H.X., R.-W.Y., Y.Z., S.J., and L.Y.; Writing – Review & Editing, L.-L.C.; Visualization, Y.-H.X., R.-W.Y., and L.-L.C.; Supervision, L.-L.C.; Funding Acquisition, L.Y. and L.-L.C.

### ACKNOWLEDGMENTS

We are grateful to G. Carmichael for reading the manuscript, D. Lafontaine for suggestions on pre-rRNA analysis, J. Chen for help in FRET assay, Y.X. He from the Core Facility Centre of the Institute of Plant Physiology and Ecology, SIBS, CAS for technical support on SIM, and all lab members for discussion. H9 cells were obtained from the WiCell Research Institute. This work was supported by CAS (XDB19020104), MOST (2016YFA0100701 and 2014CB964802), and NSFC (91440202 and 91540115).

Received: September 29, 2016

Revised: March 6, 2017

Accepted: April 6, 2017

Published: May 4, 2017

### REFERENCES

- Bierhoff, H., Dammert, M.A., Brocks, D., Dambacher, S., Schotta, G., and Grummt, I. (2014). Quiescence-induced lncRNAs trigger H4K20 trimethylation and transcriptional silencing. *Mol. Cell* 54, 675–682.
- Boisvert, F.M., van Koningsbruggen, S., Navascués, J., and Lamond, A.I. (2007). The multifunctional nucleolus. *Nat. Rev. Mol. Cell Biol.* 8, 574–585.
- Bourgeois, C.F., Mortreux, F., and Auboeuf, D. (2016). The multiple functions of RNA helicases as drivers and regulators of gene expression. *Nat. Rev. Mol. Cell Biol.* 17, 426–438.
- Calo, E., Flynn, R.A., Martin, L., Spitale, R.C., Chang, H.Y., and Wysocka, J. (2015). RNA helicase DDX21 coordinates transcription and ribosomal RNA processing. *Nature* 518, 249–253.
- Chen, L.L. (2016). Linking long noncoding RNA localization and function. *Trends Biochem. Sci.* 41, 761–772.
- Chen, X., Pan, W., Sui, Y., Li, H., Shi, X., Guo, X., Qi, H., Xu, C., and Liu, W. (2015). Acidic phospholipids govern the enhanced activation of IgG-B cell receptor. *Nat. Commun.* 6, 8552.
- Cong, L., Ran, F.A., Cox, D., Lin, S., Barretto, R., Habib, N., Hsu, P.D., Wu, X., Jiang, W., Marraffini, L.A., and Zhang, F. (2013). Multiplex genome engineering using CRISPR/Cas systems. *Science* 339, 819–823.
- Feng, W., Yonezawa, M., Ye, J., Jenuwein, T., and Grummt, I. (2010). PHF8 activates transcription of rRNA genes through H3K4me3 binding and H3K9me1/2 demethylation. *Nat. Struct. Mol. Biol.* 17, 445–450.
- Flores-Rozas, H., and Hurwitz, J. (1993). Characterization of a new RNA helicase from nuclear extracts of HeLa cells which translocates in the 5' to 3' direction. *J. Biol. Chem.* 268, 21372–21383.
- Ghoshal, K., Majumder, S., Datta, J., Motiwala, T., Bai, S., Sharma, S.M., Frankel, W., and Jacob, S.T. (2004). Role of human ribosomal RNA (rRNA) promoter methylation and of methyl-CpG-binding protein MBD2 in the suppression of rRNA gene expression. *J. Biol. Chem.* 279, 6783–6793.
- Goodfellow, S.J., and Zomerdijk, J.C. (2013). Basic mechanisms in RNA polymerase I transcription of the ribosomal RNA genes. *Subcell. Biochem.* 61, 211–236.
- Hacot, S., Coute, Y., Belin, S., Albaret, M.A., Mertani, H.C., Sanchez, J.C., Rosa-Calatrava, M., and Diaz, J.J. (2010). Isolation of nucleoli. *Curr. Protoc. Cell Biol. Chapter 3, Unit 3.36.*
- Henning, D., So, R.B., Jin, R., Lau, L.F., and Valdez, B.C. (2003). Silencing of RNA helicase II/Gualpha inhibits mammalian ribosomal RNA production. *J. Biol. Chem.* 278, 52307–52314.
- Holmström, T.H., Mialon, A., Kallio, M., Nymalm, Y., Mannermaa, L., Holm, T., Johansson, H., Black, E., Gillespie, D., Salminen, T.A., et al. (2008). c-Jun supports ribosomal RNA processing and nucleolar localization of RNA helicase DDX21. *J. Biol. Chem.* 283, 7046–7053.
- Hu, S.B., Xiang, J.F., Li, X., Xu, Y., Xue, W., Huang, M., Wong, C.C., Sagum, C.A., Bedford, M.T., Yang, L., et al. (2015). Protein arginine methyltransferase CARM1 attenuates the paraspeckle-mediated nuclear retention of mRNAs containing IRAlus. *Genes Dev.* 29, 630–645.
- Ilioka, H., Loiselle, D., Haystead, T.A., and Macara, I.G. (2011). Efficient detection of RNA-protein interactions using tethered RNAs. *Nucleic Acids Res.* 39, e53.
- Kiss, A.M., Jády, B.E., Bertrand, E., and Kiss, T. (2004). Human box H/ACA pseudouridylate guide RNA machinery. *Mol. Cell. Biol.* 24, 5797–5807.
- McStay, B. (2006). Nucleolar dominance: a model for rRNA gene silencing. *Genes Dev.* 20, 1207–1214.
- McStay, B. (2016). Nucleolar organizer regions: genomic ‘dark matter’ requiring illumination. *Genes Dev.* 30, 1598–1610.
- Nguyen, X.T., Raval, A., Garcia, J.S., and Mitchell, B.S. (2015). Regulation of ribosomal gene expression in cancer. *J. Cell. Physiol.* 230, 1181–1188.
- Ollion, J., Cochenne, J., Loll, F., Escudé, C., and Boudier, T. (2013). TANGO: a generic tool for high-throughput 3D image analysis for studying nuclear organization. *Bioinformatics* 29, 1840–1841.
- Peltonen, K., Colis, L., Liu, H., Trivedi, R., Moubarek, M.S., Moore, H.M., Bai, B., Rudek, M.A., Bieberich, C.J., and Laiho, M. (2014). A targeting modality for destruction of RNA polymerase I that possesses anticancer activity. *Cancer Cell* 25, 77–90.

- Perlaky, L., Valdez, B.C., and Busch, H. (1997). Effects of cytotoxic drugs on translocation of nucleolar RNA helicase RH-II/Gu. *Exp. Cell Res.* 235, 413–420.
- Schindelin, J., Arganda-Carreras, I., Frise, E., Kaynig, V., Longair, M., Pietzsch, T., Preibisch, S., Rueden, C., Saalfeld, S., Schmid, B., et al. (2012). Fiji: an open-source platform for biological-image analysis. *Nat. Methods* 9, 676–682.
- Schmitz, K.M., Mayer, C., Postepska, A., and Grummt, I. (2010). Interaction of noncoding RNA with the rDNA promoter mediates recruitment of DNMT3b and silencing of rRNA genes. *Genes Dev.* 24, 2264–2269.
- Schneider, D.A. (2012). RNA polymerase I activity is regulated at multiple steps in the transcription cycle: recent insights into factors that influence transcription elongation. *Gene* 493, 176–184.
- Scott, M.S., Troshin, P.V., and Barton, G.J. (2011). NoD: a Nucleolar localization sequence detector for eukaryotic and viral proteins. *BMC Bioinformatics* 12, 317.
- Seegar, T., and Barton, W. (2010). Imaging protein-protein interactions in vivo. *J. Vis. Exp.* (44), 2149.
- Sloan, K.E., Leisegang, M.S., Doebele, C., Ramírez, A.S., Simm, S., Safferthal, C., Kretschmer, J., Schorge, T., Markoutsas, S., Haag, S., et al. (2015). The association of late-acting snoRNPs with human pre-ribosomal complexes requires the RNA helicase DDX21. *Nucleic Acids Res.* 43, 553–564.
- Valdez, B.C., Henning, D., Busch, R.K., Woods, K., Flores-Rozas, H., Hurwitz, J., Perlaky, L., and Busch, H. (1996). A nucleolar RNA helicase recognized by autoimmune antibodies from a patient with watermelon stomach disease. *Nucleic Acids Res.* 24, 1220–1224.
- Warner, J.R. (1999). The economics of ribosome biosynthesis in yeast. *Trends Biochem. Sci.* 24, 437–440.
- Watkins, N.J., and Bohnsack, M.T. (2012). The box C/D and H/ACA snoRNPs: key players in the modification, processing and the dynamic folding of ribosomal RNA. *Wiley Interdiscip. Rev. RNA* 3, 397–414.
- Wu, H., Yin, Q.F., Luo, Z., Yao, R.W., Zheng, C.C., Zhang, J., Xiang, J.F., Yang, L., and Chen, L.L. (2016). Unusual processing generates SPA lncRNAs that sequester multiple RNA binding proteins. *Mol. Cell* 64, 534–548.
- Yang, L., Duff, M.O., Graveley, B.R., Carmichael, G.G., and Chen, L.L. (2011). Genomewide characterization of non-polyadenylated RNAs. *Genome Biol.* 12, R16.
- Yin, Q.F., Yang, L., Zhang, Y., Xiang, J.F., Wu, Y.W., Carmichael, G.G., and Chen, L.L. (2012). Long noncoding RNAs with snoRNA ends. *Mol. Cell* 48, 219–230.
- Zhang, Y., Forys, J.T., Miceli, A.P., Gwinn, A.S., and Weber, J.D. (2011). Identification of DHX33 as a mediator of rRNA synthesis and cell growth. *Mol. Cell. Biol.* 31, 4676–4691.
- Zhang, X.O., Yin, Q.F., Wang, H.B., Zhang, Y., Chen, T., Zheng, P., Lu, X., Chen, L.L., and Yang, L. (2014). Species-specific alternative splicing leads to unique expression of sno-lncRNAs. *BMC Genomics* 15, 287.
- Zhang, Y., Xue, W., Li, X., Zhang, J., Chen, S., Zhang, J.L., Yang, L., and Chen, L.L. (2016). The biogenesis of nascent circular RNAs. *Cell Rep.* 15, 611–624.

## STAR★METHODS

## KEY RESOURCES TABLE

REAGENT or RESOURCE	SOURCE	IDENTIFIER
<b>Antibodies</b>		
Nucleolin	Abcam	Cat#: Ab13541; RRID: AB_300442
TBRG4	Bethyl	Cat#: A301-392A; RRID: AB_938027
β-Actin	Sigma	Cat#: A3854; RRID: AB_262011
DDX21	Proteintech	Cat#: 10528-1-AP; RRID: AB_2092705
DDX21	Santa Cruz	Cat#: sc-104860; RRID: AB_2292949
RPA194	Santa Cruz	Cat#: sc-48385; RRID: AB_675814
FLAG	Sigma	Cat#: F1804; RRID: AB_262044
FLAG	Sigma	Cat#: F7425; RRID: AB_439687
DKC1	Abcam	Cat#: ab93777; RRID: AB_2245868
hnRNPU	Abcam	Cat#: ab10297; RRID: AB_297037
hnRNPL	Sigma	Cat#: R4903; RRID: AB_261966
Donkey anti-Sheep Secondary Antibody, Alexa Fluor 488 conjugate	Invitrogen	Cat#: A-11015; RRID: AB_141362
Goat anti-Rabbit Secondary Antibody, Alexa Fluor 488	Invitrogen	Cat#: A-11034; RRID: AB_2576217
Goat anti-Mouse Secondary Antibody, Alexa Fluor 555	Invitrogen	Cat#: A-21424; RRID: AB_141780
Fibrillarin	Abcam	Cat#: ab5821; RRID: AB_2105785
B23	Santa Cruz	Cat#: sc-53175; RRID: AB_630048
Goat anti-Mouse Secondary Antibody, Alexa Fluor 647	Invitrogen	Cat#: A-21236; RRID: AB_141725
<b>Chemicals, Peptides, and Recombinant Proteins</b>		
Ribonucleoside Vanadyl Complex	NEB	Cat#: S1402S
cComplete ULTRA Tablets, Mini, EASYpack Protease Inhibitor Cocktail	Roche	Cat#:000 000005892970001
5-fluorouracil (5-FU)	Sigma	Cat#: F6627
4-thiouridine (4sU)	Sigma	Cat#: T4509
EZ-link biotin-HPDP	Pierce	Cat#: 21341
Dynabeads Protein G	Invitrogen	Cat#: 1003D
Dynabeads MyOneTM Streptavidin C1	Invitrogen	Cat#: 65001
X-tremeGENE 9	Roche	Cat#: 6366236001
Lipofectamine 2000 Reagent	Thermo	Cat#: 11668019
Actinomycin D	Invitrogen	Cat#: A7592
VECTASHIELD Antifade Mounting Medium	Vector Lab	Cat#: H-1000
ProLong Gold Antifade Mountant	ThermoFisher	Cat#: P36930
TetraSpeck Microspheres, 0.1 μm	Molecular Probes	Cat#: T7279
Cyanine 3-dUTP	Enzo Life	Cat#: ENZ-42501
Hoechst 33342	Sigma	Cat#: B2261-25MG
Glutathione Sepharose 4B	GE healthcare	Cat#: 17-0756-01
Ni Sepharose 6 Fast Flow	GE healthcare	Cat#: 17-5318-01
Glycerol	ABCONE	Cat#: G46055
HEPES	ABCONE	Cat#: H33755
TWEEN 20	ABCONE	Cat#: P87875
Triton X-100	ABCONE	Cat#: X10010
Agarose	ABCONE	Cat#: A47902
Bovine Serum Albumin	ABCONE	Cat#: A23088
<b>Critical Commercial Assays</b>		
DNA-free kit	Ambion	Cat#: AM1907
DIG Northern Starter Kit	Roche	Cat#: 12039672910

(Continued on next page)

**Continued**

REAGENT or RESOURCE	SOURCE	IDENTIFIER
Mut Express MultiS Fast Mutagenesis Kit	Vazyme	Cat#: C213-01
Hieff Clone One Step Cloning Kit	Yeasen	Cat#: 10905ES25
2 × T5 Super PCR Mix	TSINGKE	Cat#: TSE005
SuperScript III Reverse Transcriptase	Invitrogen	Cat#: 18080044
RiboMAX Large-Scale RNA Production System	Promega	Cat#: P1300
Dual-Glo Luciferase Assay System	Promega	Cat#: E2980
Pierce Silver Stain for Mass Spectrometry kit	Thermo	Cat#: 24600
CellTiter 96 AQueous One Solution Cell Proliferation Assay (MTS)	Promega	Cat#: G3580
Nick Translation Kit	Abbott	Cat#: 07J00-001
Modified Bradford Protein Assay Kit	Sangon Biotech	Cat#: C503041
NuPAGE Novex 4–12% Bis-Tris Gel	Invitrogen	Cat#: NP0321BOX
StarPrep Gel Extraction Kit StarPrep	GenStar	Cat#: D205-04
Experimental Models: Cell Lines		
PA1	ATCC	Cat#: CRL-1572
HeLa	ATCC	Cat#: CCL-2
SH-SY5Y	ATCC	Cat#: CRL-2266
HEK293	ATCC	Cat#: CRL-1573
CRL-5807	ATCC	Cat#: CRL-5807
Experimental Models: Organisms/Strains		
BALB/C-nu	SLAC laboratory animal company	N/A
Recombinant DNA		
pcDNA3	Invitrogen	Cat#: A150228
pcDNA3-SLERT wt	This paper	N/A
pGL3-Basic Vector	Promega	Cat#: E1751
pGL3-rDNA-IRES	This paper	N/A
pLKO.1 puro	Addgene	Cat#: 8453
pHAGE-EF1 $\alpha$ -IRES-ZsGreen	(Chen et al., 2015)	N/A
pCMV-VSV-G	Addgene	Cat#: 8454
pMD2.G	Addgene	Cat#: 12259
pEGFP-C1-DDX21	This paper	N/A
pcDNA3-DDX21-mCherry	This paper	N/A
pEGFP-C1-RPA194	This paper	N/A
pEGFP-C1-RPA49	This paper	N/A
pET28a-DDX21	This paper	N/A
pGST-RPA194	This paper	N/A
pHAGE-EGFP-DDX21-mCherry	This paper	N/A
pHAGE-EGFP-DDX21	This paper	N/A
pHAGE-DDX21-mCherry	This paper	N/A
Software and Algorithms		
GraphPad Prism	GraphPad Software	<a href="http://www.graphpad.com/scientific-software/prism/">http://www.graphpad.com/scientific-software/prism/</a>
sgRNAs Design Tool	(Cong et al., 2013)	<a href="http://www.genome-engineering.org/">http://www.genome-engineering.org/</a>
Quantity One 1-D Software	Bio-Rad	<a href="http://www.bio-rad.com/en-us/product/quantity-one-1-d-analysis-software">http://www.bio-rad.com/en-us/product/quantity-one-1-d-analysis-software</a>
Nucleolar localization sequence Detector	(Scott et al., 2011)	<a href="http://www.compbio.dundee.ac.uk/www-nod/">http://www.compbio.dundee.ac.uk/www-nod/</a>
Fiji/ImageJ	ImageJ	<a href="https://imagej.net/Fiji/Downloads">https://imagej.net/Fiji/Downloads</a>
TANGO	N/A	<a href="http://biophysique.mnhn.fr/tango/about">http://biophysique.mnhn.fr/tango/about</a>

## CONTACT FOR REAGENT AND RESOURCE SHARING

Further information and requests for reagents should be directed to and will be fulfilled by the Lead Contact, Ling-Ling Chen ([linglingchen@sibcb.ac.cn](mailto:linglingchen@sibcb.ac.cn)).

## EXPERIMENTAL MODEL AND SUBJECT DETAILS

### Human Cell Lines

Human cell lines including PA1, HeLa, HEK293 cells were purchased from the American Type Culture Collection (ATCC; <https://www.atcc.org>).

### Subcutaneous Xenograft Tumor Models

Female nude recipient mice 4-6 weeks of age were obtained from SLAC laboratory animal company and maintained under pathogen-free conditions. Cells ( $5 \times 10^6$ ) were implanted subcutaneously in a Matrigel matrix under both sides of shoulders of each mouse and allowed to grow to reach an average size of  $\sim 30\text{-}40 \text{ mm}^2$ . Animal care and treatment were approved by the Institute Animal Care and Research Advisory Committee at SIBCB, CAS.

## METHOD DETAILS

### Plasmids Construction

Full-length *SLERT* flanked by its natural intron, splicing sites and exons was PCR amplified from the genomic DNA of PA1 cells, and the PCR product was cloned into pcDNA3 using EcoRI / NotI. All deletions and mutations of snoRNA in *SLERT* in the expression vector pcDNA3-*SLERT* wt were created using Mut Express MultiS Fast Mutagenesis Kit (Vazyme C213-01). The rDNA promoter luciferase reporter vector was constructed according to previous study (Ghoshal et al., 2004). Briefly, the Kozak sequence from pGL3-Basic Vector (Promega) was removed by Ncol and Xhol digestion and the internal ribosome entry site (IRES) was amplified from pHAGE-EF1 $\alpha$ -IRES-ZsGreen Vector and cloned into the same site with Xhol and Ncol. Then the rDNA promoter region (from -411 to +329 containing both UCE and CPE) was PCR amplified from the genomic DNA of PA1 cells and cloned into pGL3-Basic Vector using KpnI and MluI. See Table S1 for primers.

The oligonucleotides for shRNA targeting DDX21 were cloned into pLKO.1-Puro vectors. A scramble shRNA plasmid was used as a negative control. Two shRNAs (5'-CCCATATCTGAAGAAACTATT-3' and 5'-GGTGGCTCCATAGCTTT ATTT-3') produced the best knockdown efficiency. For overexpression full-length or truncated DDX21, PCR products of full-length or series truncation of DDX21 were amplified from cDNA of PA1 cells, and inserted into pHAGE-EF1 $\alpha$ -IRES-ZsGreen expression vectors with flag tag on their N-terminal.

For prokaryotic expression and purification of the His-tagged DDX21 protein, the full-length DDX21 DNA sequence was amplified from cDNAs of PA1 cells, and inserted into pET-28a vector using BamHI and NotI. For eukaryotic expression and purification of the GST-tagged RPA194, the PCR product of the full-length RPA194 DNA fused with GST was inserted into the EGFP depleted pEGFP-C1 plasmid. See Table S1 for primers.

To construct the DDX21 FRET reporter plasmid, the full-length DDX21 together with EGFP fused to its N-terminal and mCherry fused to its C-terminal, DDX21 with EGFP fused to its N-terminal, and DDX21 with mCherry fused to its C-terminal were cloned into the pHAGE expression vector that lacks IRES-ZsGreen sequences. For live cell imaging, EGFP-DDX21 and DDX21-mCherry PCR products were obtained from DDX21 reporter plasmid and cloned into pcDNA3 vector; PCR products of the full-length RPA194 and RPA49 was individually amplified from cDNA of PA1 cells and inserted into pEGFP-C1 vector. See Table S1 for primers.

### Cell Culture, Cell Transfection and Lentiviral Infection

PA1 cells were maintained in MEM $\alpha$  supplemented with 10% FBS, 1% Glutamine and penicillin/streptomycin. HeLa cells were maintained in DMEM supplemented with 10% FBS and penicillin/streptomycin. Transfection of pcDNA3 constructs was carried out with X-tremeGENE 9 (Roche) for HeLa cells (60%–70% confluence) according to the manufacturer's protocol. Lentiviral particles were produced in HEK293T cells by transient co-transfection of transfer vector constructs (pLKO.1-Puro vectors or pHAGE-EF1 $\alpha$ -IRES-ZsGreen expression vectors), pCMV-VSV-G and pMD2.G.

### Protein Expression and Purification

His-tagged full-length DDX21 in pET-28a was transformed into *E.coli* expression strain BL21 [Transetta (DE3) chemically competent cell (TRANSGEN BIOTECH, CD801)] for expression. 5 mL LB culture supplemented with 100  $\mu\text{g}/\text{L}$  kanamycin was inoculated with a single colony at 250 rpm, 37°C. After overnight growth, the culture was diluted 100-fold into 100 mL LB culture supplemented with 100  $\mu\text{g}/\text{L}$  kanamycin. Absorbance was monitored at a wavelength of 600 nm, and upon reaching an optical density (OD600) of 0.4, protein expression was induced by adding of 1 mM IPTG. After overnight incubation at 250 rpm, 16°C, cell pellets were harvested by centrifugation (5,000 rpm, 10 min, 4°C). Cell pellets were resuspended in lysis buffer (50 mM Tris pH 8.0, 300 mM NaCl, 20 mM imidazole, 1 mM PMSF) supplemented with 1 mg/ml lysozyme, and stored on ice for 30 min, followed by 10 min (5 s on/off) sonication

on ice. After centrifugation at 10,000 rpm for 30 min at 4°C, the supernatant cell lysates were incubated with Ni Sepharose (GE healthcare, 17-5318-01) for 2 hr at 4°C. The Sepharose was washed 4 times with washing buffer (50 mM Tris pH 8.0, 300 mM NaCl, 40 mM imidazole, 1 mM PMSF), and bound protein was eluted with elution buffer (50 mM Tris pH 8.0, 300 mM NaCl, 300 mM imidazole). Elution was repeated twice to gain maximum yield. The concentration of purified protein was determined by using Modified Bradford Protein Assay Kit (Sangon Biotech, C503041) and checked by SDS-PAGE.

GST-tagged full-length RPA194 in pEGFP-C1 was transfected into HEK293 cells for expression. Cells were harvested after 2 days to achieve optimal expression and purity.  $2 \times 10^8$  HEK293 cells were resuspended in lysis buffer (20 mM Tris pH 8.0, 100 mM NaCl, 1 mM PMSF, Complete EDTA free protease inhibitor (Roche), 5 mM Benzamidine) and lysed by  $2 \times 10$  s sonication. After centrifugation at 13,000 rpm for 10 min at 4°C, supernatant cell lysates were incubated with Glutathione Sepharose (GE healthcare, 17-0756-01) for 2 hr at 4°C. The Sepharose was washed 4 times with lysis buffer, and bound protein was eluted with elution buffer (50 mM Tris pH 8.0, 20 mM Glutathione). Elution was repeated twice to gain maximum yield. The concentration of purified protein was determined using Modified Bradford Protein Assay Kit (Sangon Biotech, C503041) and checked by SDS-PAGE.

### Isolation of Nucleoli

Nucleoli isolation in PA1 cells was performed as described (Hacot et al., 2010) with modifications.  $2 \times 10^7$  PA1 cells were used for nucleoli isolation. Cell pellet was suspended by gentle pipetting in 200 μL lysis buffer (10 mM Tris pH 8.0, 140 mM NaCl, 1.5 mM MgCl<sub>2</sub>, 0.5% Igepal, 2 mM Ribonucleoside Vanadyl Complex), and incubated on ice for 10 min. During the incubation, one tenth of the lysate was added to 1 mL Trizol for total RNA extraction. The rest of the lysate was centrifuged at 1000 rpm for 3 min at 4°C to pellet the nuclei and the supernatant was the cytoplasmic fraction. To fractionate nuclear fractions, nuclei pellet was resuspended with 200 μL 340 mM sucrose solution containing 5 mM MgCl<sub>2</sub>. One tenth of the lysate was added to 1 mL Trizol for nuclei RNA extraction. To prepare nucleoplasmic and nucleolar fractions, nuclei were broken by sonication until intact nuclei cannot be detected in suspension by microscope. 200 μL 880 mM sucrose solution containing 5 mM MgCl<sub>2</sub> was gently added to sonicated nuclei and then centrifuged 20 min at 2,000 rpm, 4°C to pellet nucleoli, and the supernatant was the nucleoplasmic fraction. Fractionated RNAs from the same amount of cells were used for cDNA synthesis and RT-PCR.

### RNA Isolation, qRT-PCR and Northern Blotting

Total RNA from each cultured cell line or cultured cells with different treatments was extracted with Trizol Reagent (Invitrogen) according to the manufacturer's protocol. For qRT-PCR, after treatment with DNase I (Ambion, DNA-free kit), the cDNA synthesis was carried out using SuperScript III (Invitrogen) with oligo (dT) and random hexamers. QPCR was done using SYBR Green Realtime PCR Master Mix (TOYOBO) and a StepOnePlus real-time PCR system (Applied Biosystems). The relative expression of different sets of genes was quantified to *actin* mRNA. Primer sequences for qRT-PCR and RT-PCR used were listed in Table S1.

Northern blotting was carried out according to the manufacturer's protocol (DIG Northern Starter Kit, Roche). RNA was loaded on native Agarose gels or denatured PAGE gels. Digoxigenin (Dig) labeled antisense probes were generated using T7 RNA polymerase by *in vitro* transcription with the RiboMAX Large Scale RNA Production System (Promega).

### Measurement of *SLERT* Copy Numbers

A serial dilution of the linearized plasmid pcDNA3-WT-SLERT was used qRT-PCR to generate a standard curve for *SLERT*. The copy number of the diluted plasmid pcDNA3-WT-SLERT was calculated by DNA/RNA Copy Number Calculator from website (<http://endmemo.com/bio/dnacopynum.php>). To measure the *SLERT* copy number in PA1 or H9 cells, total RNA extracted from  $2 \times 10^6$  cells of each line was reverse transcribed into cDNAs for qPCR analysis, and the copy number could be quantitated from the standard curve. See Table S1 for primers.

### RNA In Situ Hybridization and Immunofluorescence Microscopy

To detect *SLERT*, RNA FISH was carried out as previously described with *in vitro* transcribed Dig-labeled antisense probe (Yin et al., 2012). Briefly, cells were fixed with 3.6% PFA and 10% acetic acid for 15 min, followed by permeabilization with 0.5% Triton X-100 for 5 min on ice. Then cells were subjected to incubation with denatured Dig-labeled FISH probes in hybridization buffer (50% formamide in 2xSSC) at 50°C overnight. After hybridization, anti-Dig primary antibody and fluorescent secondary antibody were sequentially added to visualize signal with DeltaVision Elite imaging system (GE Healthcare). The nuclei were counterstained with DAPI. For colocalization studies, cells were co-stained with mouse anti-Nucleolin (Abcam), mouse anti-B23 (Santa Cruz Biotechnology), rabbit anti-fibrillarin (abcam), rabbit anti-DDX21 (Proteintech), and mouse anti-RPA194 (Santa Cruz Biotechnology).

### RNA/DNA Double FISH

Sequential RNA/DNA double FISH experiments were carried out after RNA FISH. Cells were denatured at 80°C for 5 min in pre-warmed 2 × SSC and 70% deionized formamide, pH 7.0. Next, cells were hybridized with denatured DNA probe prepared from Nick Translation (Abbott) overnight. After hybridization, two washes of 10 min at 37°C with 50% formamide in 2 × SSC were performed, followed by two washes of 15 min at 37°C with 1 × SSC and two washes of 15 min at 37°C with 2 × SSC. Slides were then mounted with ProLong Gold antifade reagent (Thermo Fisher SCIENTIFIC) with DAPI. Analysis was performed on single Z stacks acquired with a DeltaVision Elite imaging system (GE Healthcare). Primers for probes were listed in Table S1.

### Structured Illumination Microscopy Procedure

For all SIM experiments, cells were seeded on High Performance No.1.5 18 × 18mm glass coverslips (Schott Nexterion), fixed and permeabilized as described previously (Wu et al., 2016). 1) To visualize DDX21 and RPA194, cells were blocked with 1% BSA for 1h. Antibodies were 1:200 diluted in blocking buffer and incubated for 1 hr at RT. After washing with 1xPBS 3 times, fluorescent secondary antibodies were 1:2,000 diluted in blocking buffer and incubated for 1 hr at RT. Samples were mounted in Vectashield antifade mounting medium (Vector Lab). 2) To visualize *SLERT*, DDX21 and RPA194, cells were incubated in 50% formamide/2xSSC at RT for 10 min. A set of Cy3-labeled nick translation and denatured probes targeting *SLERT* were added and hybridize at 37°C in a humid chamber for 16 hr. Unbound probes were washed away by 50% formamide/2xSSC. For subsequent immunostaining, cells were stained as described above. 3) To visualize DDX21, RPA194 and rDNA, cells were incubated in 2xSSC at RT for 10min, then incubated with 2 µg/ml RNaseA in 2xSSC at 37°C for 1 hr. After RNaseA treatment, the samples were washed with 2xSSC for 5 times and incubated in 70% formamide/2xSSC at RT for 10 min. Then cells were denatured in prewarmed 85°C 70% formamide/2xSSC for 8 min and chill in the pre-cool 50% formamide/2xSSC on ice. A set of Cy3-labeled and denatured dsDNA probes targeting rDNA were added to the samples and hybridize at 37°C in a humid chamber for at least 16 hr. After hybridization, the samples were treated as described above to visualize DDX21 and RPA194. Primers for probes were listed in Table S1.

After performed FISH and/or IF, SIM was performed on a DeltaVision OMX V4 system (GE Healthcare) equipped with a 60 × /1.42 NA Plan Apo oil-immersion objective (Olympus) and six laser beams (405, 445, 488, 514, 568 and 642nm). The microscope was routinely calibrated with a special image registration slide and algorithm provided by GE healthcare. To obtain optimal images, immersion oil with refractive indices of 1.516 was used at 25°C room temperature. SI image stacks were captured with a z-distance of 0.125 µm and with 5 phases, 3 angles, 15 raw images per plane. The raw data were reconstructed with channel-specific OTFs and a Wiener filter was set to 0.002 for A568 and FITC channels and 0.004 for DAPI and A647 channel by using softWoRx 6.5 package (GE Healthcare). Images were registered with alignment parameters obtained from calibration measurements with 100 nm diameter TetraSpeck Microspheres with four colors (Molecular Probes).

### Structured Illumination Microscopy Imaging Analysis

All SIM images were cropped and processed by Fiji/ImageJ. Calculation of diameters of DDX21 ring-shaped structures was performed by Tango plug-in (Ollion et al., 2013). In brief, these ring-like arrangements were segmented according to a set of defaulting parameters: (1) subtract background 2D: Rolling ball method with a 10-pixel radius; (2) adaptive fast 3D filter with a 1-pixel radius in x, y, z; (3) OTSU AutoThreshold segment; (4) size filter with a minimal volume of 100 and remove objects touching x, y, z; (5) fill holes 2D. All DDX21 ring-shaped structures generated by auto-segmentation described above were manually chosen by naked eyes and only the successfully segmented rings were measured. Diameter of DDX21-rings was measured by Measure Geometrical Simple: FeretMax function in Tango plug-in.

Calculation of the integrated fluorescence intensity of pre-rRNA and the diameter of corresponding DDX21 ring-shaped structure was performed by Tango plug-in. Briefly, the reconstructed images were converted to 8 bit and imported into Tango. The DDX21-rings were segmented according to a set of defaulting parameters: (1) subtract background 2D: Rolling ball method with a 5 pixel radius; (2) choose image features by structure method with smooth scale of 0.5-pixel and integration scale of 0.5 pix; (3) OTSU AutoThreshold segment; (4) size filter with a minimal volume of 50 and remove objects touching x, y, z; (5) fill holes 2D; (6) binary close, radius = 2. All DDX21 ring-shaped structures generated by auto-segmentation described above were manually chosen by naked eyes and only the successfully segmented rings were then measured. The pre-rRNA signal in each ring was segmented as follow: (1) subtract background 2D: Rolling ball method with a 50 pixel radius; (2) OTSU AutoThreshold segment; (3) binary dilate with 2 radius in x, y, and z. The intensity of pre-rRNA was measured by integrated density of signal quantification function and the diameter of each DDX21 ring-like structure was measured by Measure Geometrical Simple: FeretXY function. See Figures S5A and 5C.

The measurement of integrated fluorescence intensity of corresponding *SLERT* is similar as above, but without the post-filters of binary dilate for a more accurate calculation for overlapping *SLERT* signal on individual DDX21-rings. Of note, the data exported from Tango was then regressed by SPSS using the power function as follow:  $y = ax^b$ , where y denotes the diameter of DDX21-ring while x denotes the integrated fluorescence intensity of *SLERT* on the correspondent ring. The significance test of the nonlinear regression was performed after taking the log of both x and y, which is a linearization procedure of the nonlinear regression. See Figures S5B and 5G.

### Live Cell Imaging

All live cell imaging was carried out on a DeltaVision Elite imaging system (GE Healthcare), equipped with a 60 × /1.42 NA Plan Apo oil-immersion objective, 100 × /1.40 NA Plan Apo oil-immersion objective (Olympus) and live cell imaging environment control system (Live Cell Instrument). Cells were cultured on 29 mm No.1.5 glass bottom dishes (Cellvis). DDX21-EGFP, DDX21-mCherry, EGFP-RPA194/DDX21-mCherry or EGFP-RPA49/DDX21-mCherry was transfected into cells 48 hr prior to imaging by X-tremeGENE 9 (Roche). Cells were washed once with PBS and the medium was replaced by FluoroBrite DMEM (GIBCO) supplemented with 10% FBS and 4 mM GlutaMax supplement and placed back in the incubator for 1 hr. For imaging of the single time point, six z sections with 0.2 µm spacing were acquired and for imaging of time lapse, cells were imaged in single layer per 15 s for single channel or per 30 s for double channels. For presentation in figures, raw data were deconvoluted by softWoRx 6.5 using the enhanced ratio method and cropped by Fiji/ImageJ (Schindelin et al., 2012).

### **Knockout SLERT by CRISPR/CAS9**

Two sgRNAs (5'-CATGAGTCACAGTGTCTG-3' and 5'-ATGAGCTGTG GAGCTTGCTG-3') that target the box H of SNORA5A and SNORA5C respectively were individually inserted into PX330 plasmid (Addgene). Transfection plasmids in PA1 cells was carried out with Lipofectamine 2000 Reagent (Thermo) according to the manufacturer's instructions. Genomic DNA and total RNA of selected single clones were extracted either for the genotyping validation with appropriate sets of primer listed in [Table S1](#) or for knockout efficiency validation by qRT-PCR and Northern blotting in [Figures 2A–2C, S1H](#), and [S1I](#).

### **Collection and Quantification of Nascent pre-rRNA**

PA1 cells ( $1 \times 10^7$ ) were pretreated with 20  $\mu\text{M}$  5-fluorouracil (5-FU) for 3 hr to halt rRNA processing ([Zhang et al., 2011](#)) and pulse-chased with 100  $\mu\text{M}$  4-thiouridine (4sU) to monitor nascent pre-rRNA levels in the last 30 min period. Total RNA was extracted and used for biotinylation and purification of 4sU-labeled nascent RNA. 100–140  $\mu\text{g}$  4sU-labeled total RNA was incubated in biotinylation buffer (10 mM Tris pH 7.4, 1 mM EDTA) with 0.2 mg/ml EZ-link biotin-HPDP (Pierce, 21341), which was dissolved in dimethylformamide (DMF, Sigma, D4551) at a concentration of 1 mg/ml at room temperature for 1.5 hr with rotation. Unbound biotin-HPDP was removed by equal volume chloroform extraction twice, and RNA was precipitated at 13,000 rpm for 15 min at 4°C with 1:10 volume of 5 M NaCl and an equal volume of isopropanol. The RNA pellet was washed twice with 75% ethanol and resuspended in 150  $\mu\text{L}$  DEPC•H<sub>2</sub>O. RNA quality was checked by electrophoresis analysis to exclude RNA degradation. 4sU-labeled and unlabeled RNA was separated using streptavidin-coated magnetic beads (Invitrogen). Biotinylated RNA was incubated with 150  $\mu\text{L}$  Streptavidin beads at room temperature for 20 min. Beads were washed four times with 0.9 mL of 65°C washing buffer (100 mM Tris pH 7.4, 10 mM EDTA, 1 M NaCl, 0.1% Tween 20), followed by four times with 0.9 mL of room temperature washing buffer. Nascent RNA was eluted with 100  $\mu\text{L}$  0.1 M dithiothreitol (DTT) twice, and RNA was precipitated with 40  $\mu\text{L}$  of 4 M LiCl, 2  $\mu\text{L}$  glycogen and 600  $\mu\text{L}$  ice-cold ethanol.

### **Dual Luciferase Reporter Assay**

For rDNA promoter luciferase assay, *SLERT* KO cells and control cells were seeded in 96-well plate and co-transfected with pGL3-rDNA-IRES reporter and Renilla luciferase vector using Lipofectamine 2000 Reagent (Invitrogen). The transfection ratio of pGL3-rDNA-IRES and the Renilla luciferase vector was 4:1, and the Renilla luciferase vector was used as an internal control for normalization. 24 hr after transfection, the luciferase activity was measured using Dual-Glo Luciferase Assay System (Promega) according to manufacturer's instructions.

### **Ribosome Fractionation**

*SLERT* KO and control cells were exposed to cycloheximide (100  $\mu\text{g}/\text{ml}$ ) for 15 min, then  $2 \times 10^7$  cells were lysed in 500  $\mu\text{L}$  lysis buffer containing 20 mM Tris pH 7.4, 15 mM MgCl<sub>2</sub>, 200 mM KCl, 1% Triton X-100, 100  $\mu\text{g}/\text{ml}$  cycloheximide, 1 mM DTT, 1 mg/ml heparin and 40 U/ mL RNasin (Promega). The samples were centrifuged at 13,000 rpm at 4°C for 10 min. For fractionation, the lysates were loaded on 15%–45% sucrose gradients and separated by ultracentrifugation with a SW41 rotor (Beckman) at 36,000 rpm at 4°C for 2.5 hr. Linear sucrose gradients were prepared with a Gradient Master (Biocomp) as indicated by the manufacturer. The distribution of ribosomes on the gradients was recorded using BIOCOMP Piston Gradient Fractinator equipped with BIO-RAD ECONO UV Monitor (set at 254 nm).

### **tRSA RNA Pull-down Assay and Western Blotting**

tRSA RNA pull-down assays were carried out as described ([Iioka et al., 2011](#)) with modifications. *SLERT* full-length or internal sequence was cloned into pcDNA3 plasmid with the tRSA tag at its 5' end. RNA products were *in vitro* transcribed using the T7 RiboMAX Large-Scale RNA Production System (Promega). 10  $\mu\text{g}$  per reaction of synthetic RNAs were denatured for 5 min at 65°C in RNA Structure buffer (10 mM HEPES pH 7.0, 10 mM MgCl<sub>2</sub>) and slowly cooled down to room temperature. Then, folded RNAs were incubated with 50  $\mu\text{L}$  of streptavidin Dynabeads (Invitrogen) for 20 min at 4°C in the presence of 2 U/ml RNasin (Promega). PA1 cells ( $1 \times 10^7$ ) were harvested and resuspended in 1 mL of lysis buffer [10 mM HEPES pH 7.0, 200 mM NaCl, 1 mM DTT, 1% Triton X-100, protease inhibitor cocktail (Roche)] followed by sonication for 4 × 10 s with an interval of 1 min on ice and then centrifuged at 13,000 rpm for 10 min at 4°C. The supernatant was pre-cleared with 50  $\mu\text{L}$  of streptavidin Dynabeads for 20 min at 4°C followed by the addition of 20  $\mu\text{g}/\text{ml}$  yeast tRNA for 20 min at 4°C. Then the pre-cleared lysate was added to folded RNAs and incubated for 3.5 hr at 4°C followed by washing 4 × 5 min with wash buffer [10 mM HEPES pH 7.0, 400 mM NaCl, 1 mM DTT, 1% Triton X-100, protease inhibitor cocktail (Roche), 2 mM RVC]. To harvest the protein complex, 50  $\mu\text{L}$  of 1 × SDS loading buffer was added and boiled for 10 min at 100°C. Retrieved proteins were analyzed by WB with primary antibodies anti-DKC1 (Abcam), anti-DDX21 (Proteintech) and anti-hnRNP U (abcam).

### **Silver Staining and Mass Spectrometry**

After tRSA pull-down, equal amounts of proteins were loaded on NuPAGE 4%–12% Bis-Tris Gel (Invitrogen). Then the gel was stained using Pierce Silver Stain for Mass Spectrometry kit (Thermo Fisher Scientific) according to the manufacturer's instructions. After silver staining, specific bands were cut and sent to Core Facility of Molecular Biology (Institute of Biochemistry and Cell Biology, Shanghai, CAS) for mass spectrometry analysis.

### Native RNA-Protein Complex Immunoprecipitation

PA1 cells ( $1 \times 10^7$ ) were harvested, resuspended in 1 mL lysis buffer [50 mM Tris pH 7.4, 150 mM NaCl, 0.05% Igepal, 0.5% NP-40, 0.5 mM PMSF, 2 mM RVC, protease inhibitor cocktail (Roche)] followed by  $4 \times 10$  s sonication with an interval of 1 min on ice. After centrifuging at 13,000 rpm for 10 min at 4°C, the supernatant was pre-cleared with 15 µL Dynabeads Protein G (Invitrogen). The pre-cleared lysates were further incubated with 2 µg anti-DDX21 antibody (Proteintech) for 2 hr at 4°C. Then 15 µL Dynabeads Protein G beads (blocked with 1% BSA and 20 µg/ml yeast tRNA) were added to the mixture and incubated for another 1 hr at 4°C followed by washing with wash buffer [50 mM Tris pH 7.4, 300 mM NaCl, 0.05% Sodium Deoxycholate, 0.5% NP-40, 0.5 mM PMSF, 2 mM RVC, protease inhibitor cocktail (Roche)]. The RNA-protein complex was eluted with elution buffer (100 mM Tris pH 6.8, 4% SDS) at room temperature for 15 min. For qRT-PCR, each RNA sample was treated with DNase I (Ambion, DNA-freeTM kit) and then reverse transcription was performed with SuperScript III Reverse Transcriptase (Invitrogen) with oligo (dT) and random hexamers followed by qRT-PCR analysis. Primers were listed in [Table S1](#).

### Formaldehyde Crosslinking RNA Immunoprecipitation

PA1 cells ( $1 \times 10^7$ ) were harvested and suspended in 10 mL PBS with 1% formaldehyde to fix 10 min at room temperature. Cross-linking was stopped by the addition of glycine to a final concentration of 0.25 M followed by incubation at room temperature for 5 min. After pelleting cells at 1,000 rpm for 5 min, the cell pellet was resuspended in 1 mL RIPA buffer [50 mM Tris pH 7.4, 150 mM NaCl, 1% NP-40, 0.5% Sodium Deoxycholate, 1 mM PMSF, 2 mM RVC, protease inhibitor cocktail (Roche)] followed by  $8 \times 10$  s sonication with an interval of 1 min on ice. After centrifuging at 13,000 rpm for 10 min at 4°C, the supernatant was pre-cleared with 15 µL Dynabeads Protein G (Invitrogen) and 20 µg/ml yeast tRNA at 4°C for 30 min. Then the pre-cleared lysate was incubated with beads that were pre-coated with 2 µg anti-DDX21 antibody (Proteintech) for 4 hr at 4°C. The beads were washed  $4 \times 5$  min with washing buffer I (50 mM Tris pH 7.4, 1 M NaCl, 1% NP-40, 1% Sodium Deoxycholate), and  $4 \times 5$  min with washing buffer II (50 mM Tris pH 7.4, 1 M NaCl, 1% NP-40, 1% Sodium Deoxycholate, 1 M Urea). The complex was eluted from beads by adding 140 µL elution buffer (100 mM Tris pH 8.0, 10 mM EDTA, 1% SDS). To reverse crosslinking, 4 µL 5 M NaCl and 2 µL 10 mg/ml proteinase K were added into the RNA samples, and incubated at 42°C for 1 hr followed by another hour incubation at 65°C. RNA was then extracted, digested with DNase I (Ambion) and used to synthesize cDNA with SuperScript III Reverse Transcriptase (Invitrogen) with oligo (dT) and random hexamers followed by qRT-PCR analysis. Primers were listed in [Table S1](#).

### Co-Immunoprecipitation

PA1 cells or PA1 cells expressing flag-DDX21 or flag-DDX21 truncations ( $2 \times 10^7$ ) were harvested and suspended in 1 mL lysis buffer [50 mM Tris pH 7.4, 150 mM NaCl, 0.05% Igepal, 0.5% NP-40, 0.5 mM PMSF, 2 mM RVC, protease inhibitor cocktail (Roche)] followed by  $3 \times 10$  s sonication. After incubation with 2 µg anti-DDX21 antibody (Santa Cruz) or anti-flag M2 antibody (Sigma), the beads were washed  $4 \times 5$  min with wash buffer [50 mM Tris pH 7.4, 300 mM NaCl, 0.05% Sodium Deoxycholate, 0.5% NP-40, 0.5 mM PMSF, 2 mM RVC, protease inhibitor cocktail (Roche)]. To harvest the protein complex, 50 µL of 1 × SDS loading buffer (62.4 mM Tris pH 6.8, 10% glycerol, 2% SDS, 0.0012% bromophenol blue) was added, boiled for 10 min at 100°C, and analyzed by western blotting.

### In vitro Competition Binding Assay

Ni Sepharose (GE Healthcare) was washed twice and resuspended with 1 mL binding buffer [50 mM Tris pH 7.4, 150 mM NaCl, 0.1 mM DTT, 0.5 mM PMSF, 2 mM RVC, protease inhibitor cocktail (Roche)]. Then 10 pmol each of His-DDX21 and GST-PRA194 purified proteins were added to the washed Ni Sepharose, together with or without 10 pmol or 50 pmol RNAs. The binding reactions were incubated 1 hr at 4°C, followed by 3 times washing with 1 mL binding buffer. To harvest the protein complex, 50 µL of 1 × SDS loading buffer was added and boiled for 10 min at 100°C. Retrieved proteins were analyzed by WB.

### Dig-Labeled RNA Pull-down Assay

Dig-RNA pull-down assays were carried out as described ([Hu et al., 2015](#)) with modifications.  $2 \times 10^7$  PA1 cells or PA1 cells expressing flag-DDX21 or flag-DDX21 truncations were used to immunoprecipitate with either anti-DDX21 (Santa Cruz) or anti-flag M2 (Sigma) antibodies. After immunoprecipitation and wash, one-fourth beads was saved for WB. The rest was equilibrated in binding buffer [50 mM Tris-HCl at pH 7.4, 150 mM NaCl, 0.05% Igepal, 0.5% NP-40, 0.5 mM PMSF, 2 mM RVC, protease inhibitor cocktail (Roche)] and incubated with 300 ng of Dig-labeled RNA for 4 hr at 4°C. For SLERT truncations, the same mole transcripts were used for protein binding assay. After washing  $4 \times 5$  min with binding buffer, the bound RNAs were extracted and analyzed by denatured PAGE gel.

### Electrophoretic Mobility Shift Assay

The Dig-labeled RNAs were annealed by heating at 65°C for 5 min, then slowly cool down to room temperature. 1 fmol of the labeled RNAs were used for each EMSA reaction. Protein-RNA binding was carried out with indicated amount of purified protein and annealed Dig-labeled RNA in binding buffer [100 mM HEPES pH 7.5, 200 mM KCl, 10 mM MgCl<sub>2</sub>, 10 mM DTT (DL-Dithiothreitol)]. Binding reactions were incubated at room temperature for 25 min, then immediately loaded onto a 8% nondenaturing polyacrylamide 0.5 × TBE gel. The gel was transferred to nylon membrane, and imaged by incubation with Anti-Digoxigenin-AP Solution.

### Förster Resonance Energy Transfer Assay

FRET efficiency was measured with donor dequenching approach as described (Seegar and Barton, 2010) with modifications. *SLERT* KO and control PA1 cells were infected with DDX21 FRET reporter lentivirus. 24 hr later, cells were fed with pre-warmed fresh medium and then infected the second time with the same virus on the plates. 2 days after the 1st infection, cells were treated with trypsin, and plated on glass coverslips growing for another 24 hr. After fixing with 4% PFA for 10min at room temperature, the coverslips were mounted on the slide and ready for Confocal imaging analysis. Cell imaging was performed on a Leica TSC SP8 STED 3X confocal laser scanning microscope (Leica) with Leica software acceptor photo-bleaching program. In brief, zooming onto cells of interest, highlighting an ROI (region of interest) in which the photo-destruction of the acceptor (mCherry) occurred and began the program. For photo-destruction of the acceptor, cells were photo-bleached with 561 nm laser line (set at 100% intensity, 5 times). The images were captured in both channels before and after photo bleaching. In all experiments, about 30 cells were measured, and FRET efficiency was calculated as  $E = (1 - \text{Pre}/\text{Post}) \times 100\%$ , where Pre and Post represent the intensity of donor (EGFP) fluorescence before and after photo bleaching.

### Chromatin Immunoprecipitation

PA1 cells ( $1 \times 10^7$ ) were harvested and suspended in 10 mL PBS with 1% formaldehyde to fix 10 min at room temperature. Cross-linking was quenched by the addition of glycine to a final concentration of 0.25 M followed by incubation at room temperature for 5 min. After pelleting cells at 1,000 rpm for 5 min, the cell pellet was resuspended in 1 mL lysis buffer (50 mM Tris pH 8.0, 150 mM NaCl, 5 mM EDTA, 1% Triton X-100, 0.1% Sodium Deoxycholate) followed by sonication with S220 Focused-ultrasonicators (Covaris) to achieve 300-500 bp DNA fragments. After centrifugation at 16,000 g for 10 min at 4°C, the supernatant was pre-cleared with 15 µL Dynabeads Protein G (Invitrogen) with 100 µg BSA and 100 µg ssDNA. Then the precleared lysates were incubated overnight at 4°C with 2 µg anti-Pol I antibody (Santa Cruz) or anti-DDX21 (Proteintech). The beads were washed with 600 µL lysis buffer, 600 µL high salt wash buffer (1% Triton X-100, 0.1% Sodium Deoxycholate, 50mM Tris-HCl at pH8.0, 0.5 M NaCl, 5 mM EDTA), 600 µL LiCl immune complex wash buffer (0.25 M LiCl, 0.5% Igepal, 0.5% Sodium Deoxycholate, 10 mM Tris pH 8.0, 1 mM EDTA) sequentially, followed by two washes with 600 µL TE Buffer (10 mM Tris pH 8.0, 1 mM EDTA) at 4°C. The complex was eluted by adding 200 µL fresh-prepared elution buffer (1% SDS, 0.1 M NaHCO<sub>3</sub>) with rotation at room temperature for 15 min. Then the reverse crosslinking was carried out by adding 8 µL 5 M NaCl and incubated at 65°C for 4 hr, followed by supplemented with 4 µL 0.5 M EDTA and 10 µL proteinase K (10 mg/ml) at 55°C for 2 hr. DNAs were purified by phenol/chloroform extraction and ethanol precipitation by adding 20 µg yeast tRNA. The pellets were dissolved in 100 µL ddH<sub>2</sub>O for qRT-PCR. Primers were listed in Table S1.

### Soft Agar Colony Formation Assay

In 6-well plates, 2 mL bottom layer medium (1% agarose and 10% FBS) was added to per well and cooled down for 0.5h at room temperature. Then 2 mL top layer medium (0.8% agarose and 20% FBS) mixed with  $5 \times 10^3$  cells were added to each well and cooled down for 10 min at 4°C. The cells were cultured at 37°C for 3 weeks. Then 1 mL 0.005% Crystal Violet was added to each well for 1h at room temperature for pictures and the average number of colonies per well were shown. Colonies were counted with a Zeiss LSM 510 microscope.

### Cell Proliferation Assay

$3 \times 10^3$  *SLERT* OE and control cells were seeded in 96-well and cell numbers were measured every 24h according to CellTiter 96 AQueous One Solution Cell Proliferation Assay (Promega). Data were presented with respect to 0h cells set to a value of 1.

### QUANTIFICATION AND STATISTICAL ANALYSIS

Data were analyzed using Student's t test or Mann-Whitney Test by GraphPad Prism 6 software. Statistical significance is defined as: \* p < 0.05, \*\* p < 0.01 and \*\*\* p < 0.001. Error bars represent SD in triplicate experiments. Regression analysis was performed by GraphPad Prism 7 software. See figure legends for details.

# Supplemental Figures

Cell

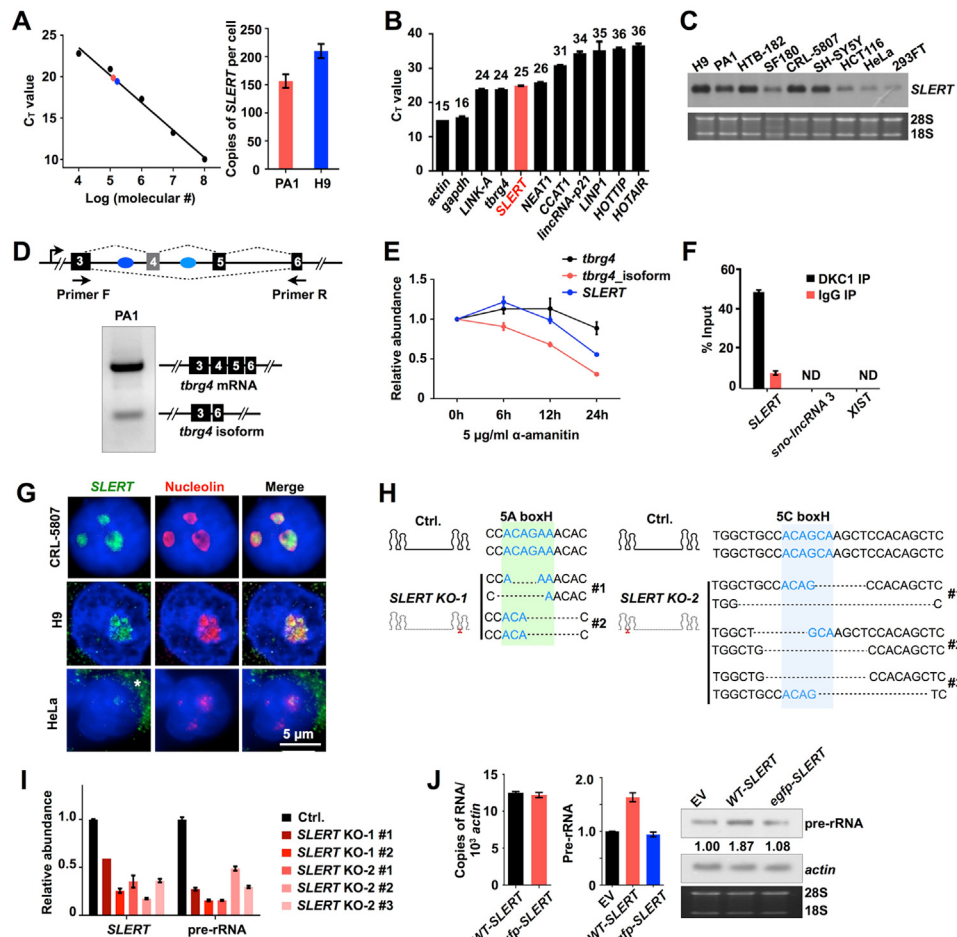


**Figure S1. Characterization of SLERT, Related to Figures 1 and 2**

- (A) The copy number of SLERT per cell in PA1 and H9 cells. Left, the linear relationship between the log SLERT copy number and its C<sub>T</sub> value by qRT-PCR. Black dots represent known copies of SLERT from a plasmid DNA containing SLERT sequences and the red and blue dots represent SLERT copies in examined cells. Right, the average copies of SLERT per cell.
- (B) The relative abundance of SLERT (red) in PA1 cells. The Ct value of each RNA was shown and the primer sets used to determine each lncRNA were from published studies.
- (C) SLERT is highly expressed in a number of human cell lines, revealed by NB with a probe shown in Figure 1A. 28S and 18S rRNA were used as loading controls.
- (D) Alternative splicing of tbrg4 pre-mRNA in PA1 cells. Semiquantitative RT-PCR with primers targeting the exons 3 and 6 of TBRG4 showed two major bands in Agarose gel. The longer isoform contains exons 3-6 of TBRG4 and the shorter one contains exons 3 and 6.
- (E) The half-lives of the full-length tbrg4 mRNA, the tbrg4 isoform with exons 4 and 5 skipped and SLERT. PA1 cells were treated with 5 µg/ml α-amanitin for different times and the total RNA was extracted and analyzed by qRT-PCR.
- (F) Formaldehyde cross-linking RIP of DKC1. The assay was performed in PA1 cells using anti-DKC1 or anti-IgG antibodies followed by qRT-PCR. XIST and one box C/D snoRNA-ended sno-lncRNA were used as controls. The percentage of RIP-enriched RNA relative to input was calculated. N.D., not detected.
- (G) SLERT localizes to the nucleolus. Co-staining of SLERT (green) and the nucleolar marker protein Nucleolin (red) in CRL-5807 (upper panels), H9 (middle panels) and HeLa cells (bottom panels). Of note, the ISH probe recognizes the internal sequence of SLERT also detects the exon 4 in tbrg4 mRNA (Figure 1B). Long exposure time was applied to visualize the low expressed endogenous SLERT in HeLa cells, which resulted in signals of cytoplasmic tbrg4 mRNA (white asterisk).
- (H) SLERT KO by CRISPR/CAS9 in PA1 cells. Each sgRNA targets the box H of each snoRNA, the minimal sequence that is required for SLERT formation (see Figure 1D). Several single clones carrying the indicated deletion in double alleles were identified.
- (I) SLERT KO led to significantly reduced pre-rRNA production. Total RNA was extracted and analyzed by qRT-PCR. Data were normalized to actin mRNA.
- (J) The internal sequence of SLERT promoted pre-rRNA transcription. Left, qRT-PCR revealed the relative expression level of the WT- and egfp-SLERT in WT- and egfp-SLERT OE cells. Middle, overexpression of wt-, but not egfp-SLERT, led to increased pre-rRNA production in PA1 cells, as revealed by qRT-PCR. Data were normalized to actin mRNA. Right, overexpression of wt-, but not egfp-SLERT led to increased pre-rRNA production, as revealed by NB. The relative levels of pre-rRNA were determined using Quantity One and labeled underneath.
- In (A), (B), (E), (F), (I), and (J), error bars represent SD in triplicate experiments.

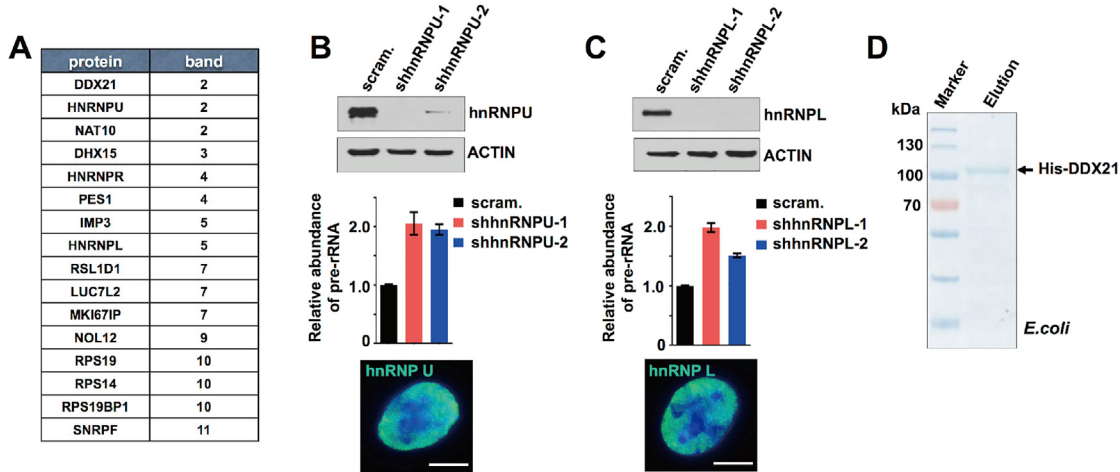


**Figure S2. Identification of *SLERT*-Associated Proteins, Related to Figure 3**

(A) MS results of *SLERT* pull-down. Identified candidate proteins by mass spectrum and their corresponding bands in the silver staining of *SLERT* tRSA pull down shown in Figure 3B.

(B) Knockdown of hnRNP U (top panels, WB) led to increased pre-RNA expression (the middle panel, qRT-PCR, normalized to actin mRNA). However, hnRNP U is largely distributed in the nucleoplasm in PA1 cells (bottom, a representative image of hnRNP U). Scale bar, 5  $\mu$ m.

(C) Knockdown of hnRNP L (top panels, WB) led to increased pre-RNA expression (the middle panel, qRT-PCR, normalized to actin mRNA). However, hnRNP L is primarily located in the nucleoplasm in PA1 cells (bottom, a representative image of hnRNP L). Scale bar, 5  $\mu$ m.

(D) Purification of His-DDX21 in *E.coli*. The purified His-DDX21 was revealed by SDS-PAGE and Coomassie Blue staining.

In (B) and (C), error bars represent SD in triplicate experiments.

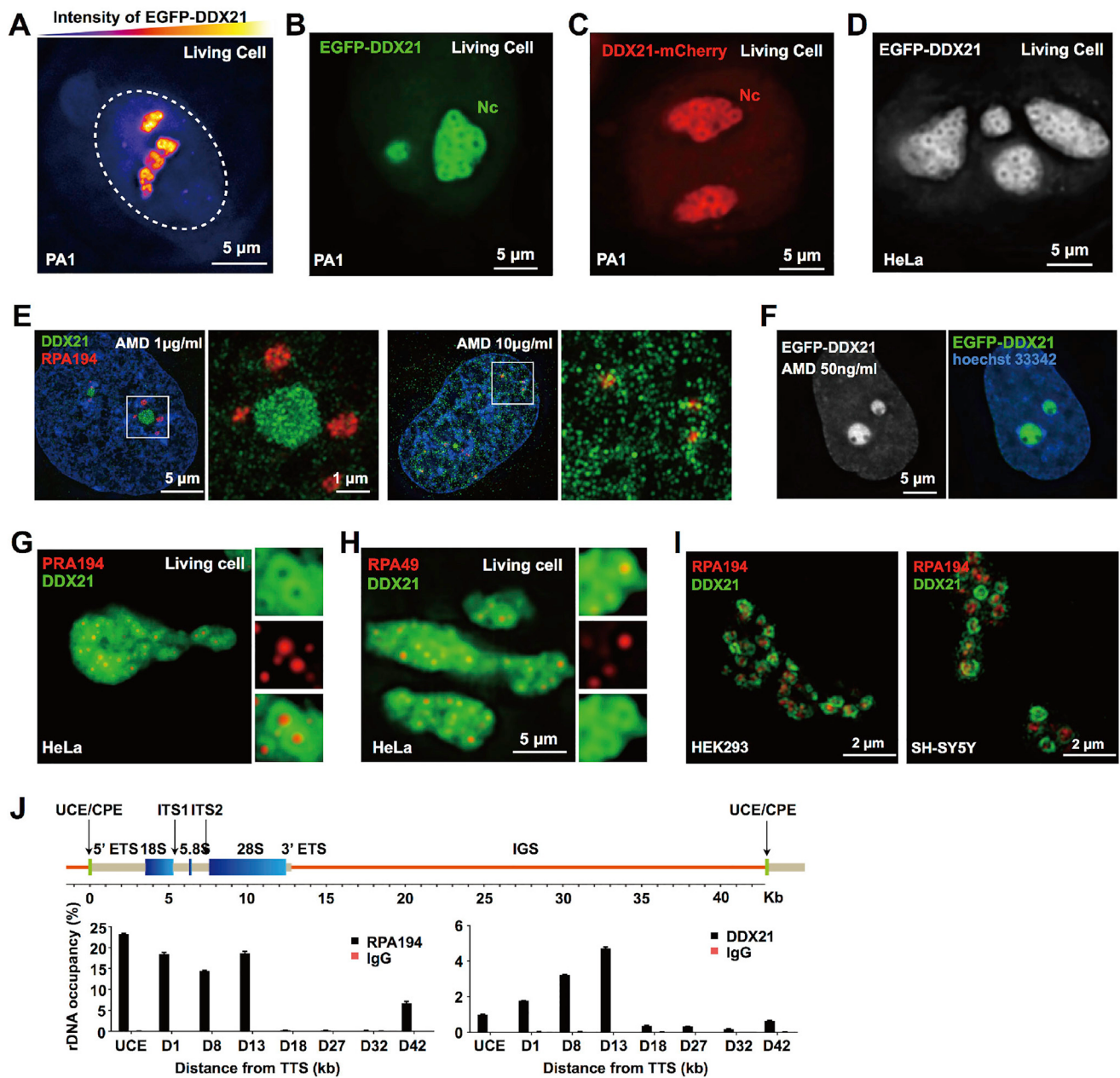


**Figure S3. DDX21 Forms Ring-like Structures Surrounding the Pol I Complexes, Related to Figure 4**

(A) EGFP-DDX21 was mainly localized in the nucleolus in living PA1 cells. EGFP-DDX21 transfected into PA1 cells imaged by a WF microscope was shown in pseudocolor.

(B) EGFP-DDX21 assembles into DDX21-ring patterns in the nucleolus in live PA1 cells. EGFP-DDX21 transfected into PA1 cells imaged by a live cell deconvolution imaging system was shown.

(C) DDX21-mCherry assembles into DDX21-ring patterns in the nucleolus in live PA1 cells. DDX21-mCherry transfected into PA1 cells imaged by a live cell deconvolution imaging system was shown.

(D) EGFP-DDX21 assembles into DDX21-ring patterns in the nucleolus in living HeLa cells. EGFP-DDX21 transfected into HeLa cells imaged by a live cell deconvolution imaging system was shown in pseudocolor.

(E) DDX21-rings were disrupted by Pol I transcription inhibition. Immunofluorescence images of the endogenous DDX21 (green) and RPA194 (red) by SIM in PA1 cells pretreated with different concentrations of Pol I transcription inhibitor AMD for 3h. Note that a higher AMD concentration disrupted both the nucleolar localization and the ring-shaped structures of DDX21 molecules.

(F) DDX21-rings were disrupted by Pol I transcription inhibition, revealed by live cell analysis in PA1 cells. Nucleolus was stained with Hoechst 33342.

(G and H) RPA194 or RPA49 is surrounded by DDX21-rings in living HeLa cells. EGFP-RPA194 or RPA49 (red) and DDX21-mCherry (green) in living HeLa cells imaged by a live cell deconvolution imaging system was shown in pseudocolor.

(legend continued on next page)

(I) The Pol I complexes are located in the center of DDX21-rings in HEK293 (left) and SH-SY5Y (right) cell lines. Immunofluorescence images of the endogenous DDX21 (green) and RPA194 (red) by SIM in HEK293 or SH-SY5Y was shown.

(J) RPA194 and DDX21 occupancies at rDNAs. Top, a schematic drawing of one rDNA cluster. Bottom, ChIP-qPCR analysis of the RPA194 and DDX21 genomic occupancies at the rDNA locus in PA1 cells. See [Figure 6G](#) for details. Error bars represent SD in triplicate experiments.

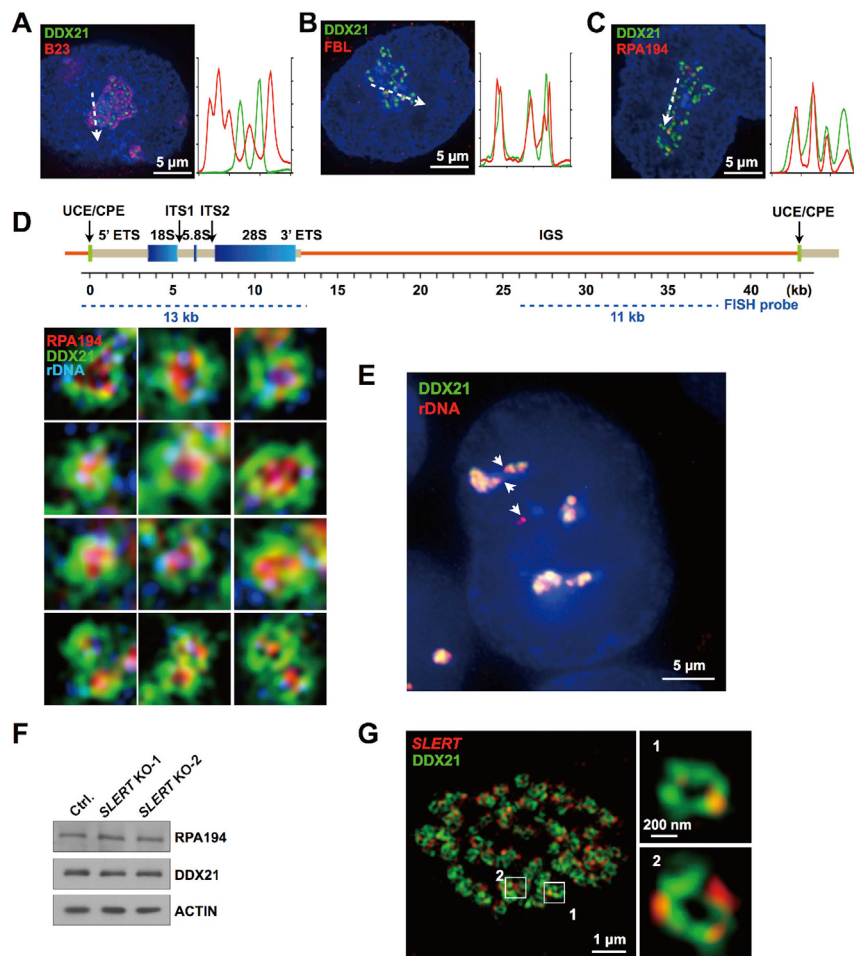


**Figure S4. The DDX21 Rings Are Assembled at the Border of FC and DFC in the Transcriptionally Active NORs, Related to Figure 5**

(A–C) Co-localization analysis of DDX21 with marker proteins of three subregions of the nucleolus in PA1 cells. (A) DDX21 (green) and the marker protein for GC, B23 (red). (B) DDX21 (green) and the marker protein for DFC, Fibrillarin (red). (C) DDX21 (green) and the marker protein for FC, RPA194 (red). The respective plot profile of each image was also shown.

(D) rDNA repeats were engaged to Pol I complexes surrounded by DDX21-rings. Representative images of co-staining DDX21 (green), RPA194 (red) and rDNAs (blue) by SIM in PA1 cells were shown. The FISH probe to detect the rDNA repeats was shown on top.

(E) DDX21-ring structures were associated with active Pol I transcription. A representative wide field image of co-staining DDX21 (green) and rDNAs (red) in PA1 cells was shown. Nucleus was shown by DAPI staining. Of note, white arrow heads indicate the non-overlapping DDX21 signals with rDNAs.

(F) WB revealed SLERT KO has no detectable effect on the expression of RPA194 and DDX21 proteins.

(G) The localization pattern of SLERT and DDX21-rings. A representative image of co-staining DDX21 (green) and SLERT (red) by SIM in PA1 cells was shown.

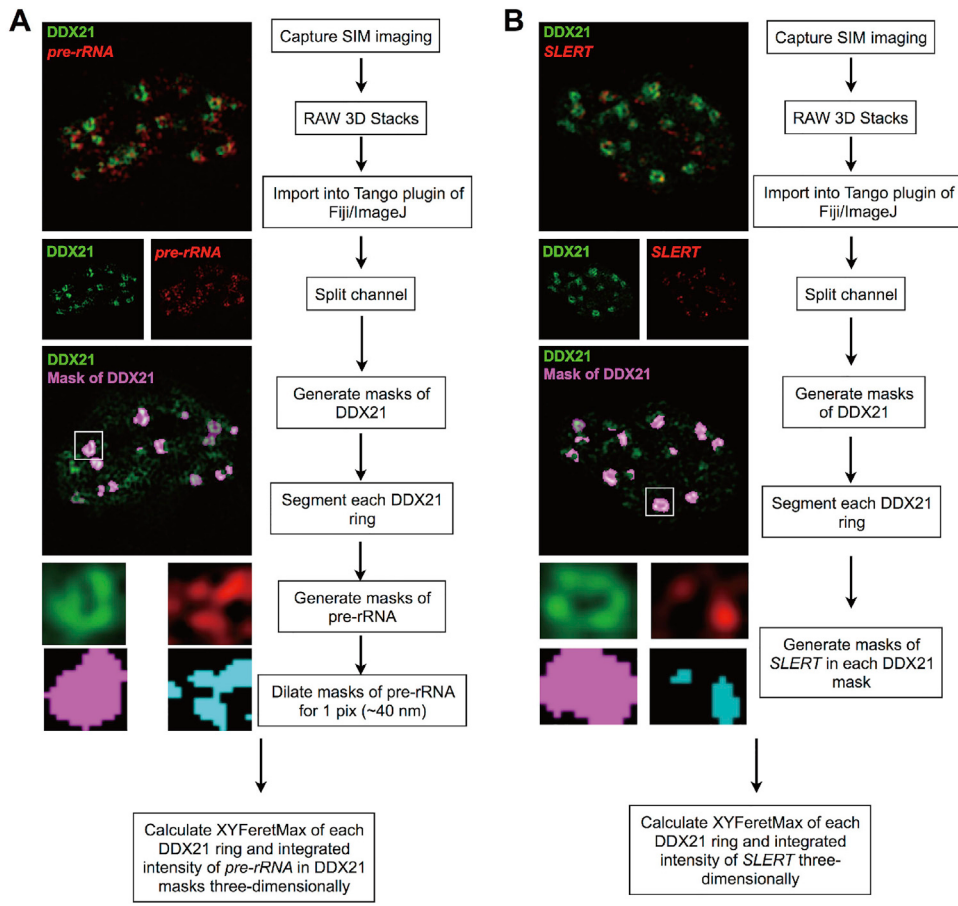


**Figure S5. Schematic Drawings to Illustrate the Experimental Flow for Figures 5C and 5G, Related to Figure 5**

(A and B) The raw SIM data were imported, masked, and segmented in Tango plugin of Fiji/ImageJ for each channel followed by intensity and XYFeretMax calculation. See the [STAR Methods](#).

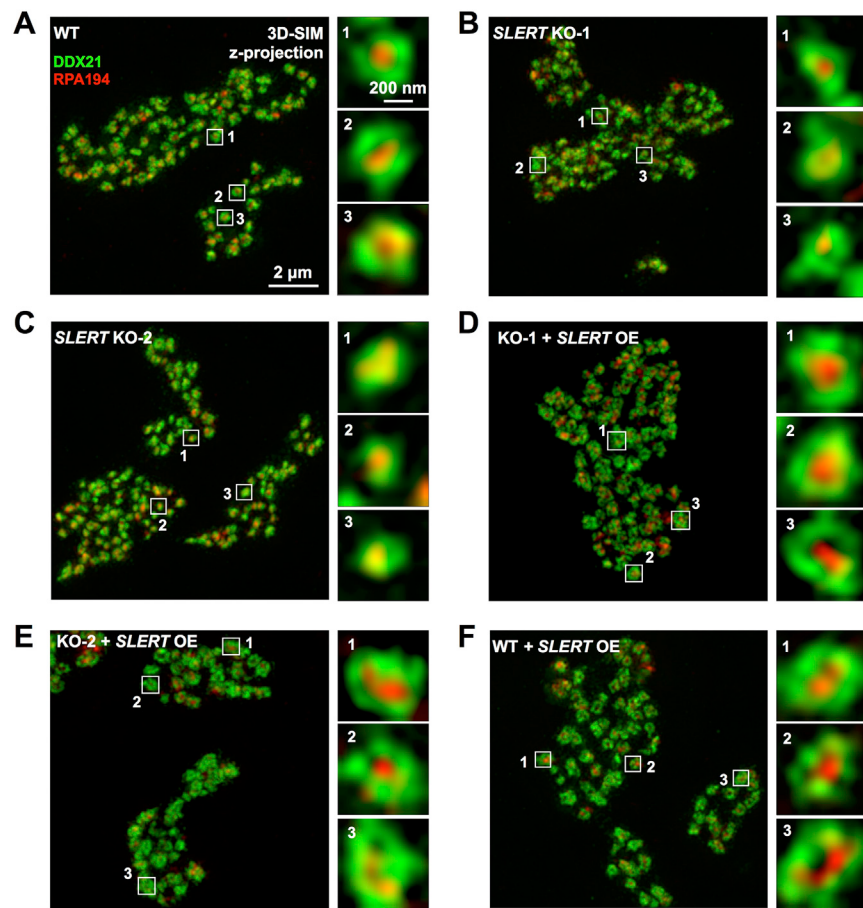


**Figure S6. SLERT Modulates the Conformational Change of DDX21 Rings, Related to Figure 5**

Co-staining of DDX21 (green) and RPA194 (red) in WT (A), SLERT KO (B,C), SLERT KO with WT-SLERT rescue (D,E) and WT with WT-SLERT overexpression (F). Left, z-projection of images. Right, single layer of images of representative cells.

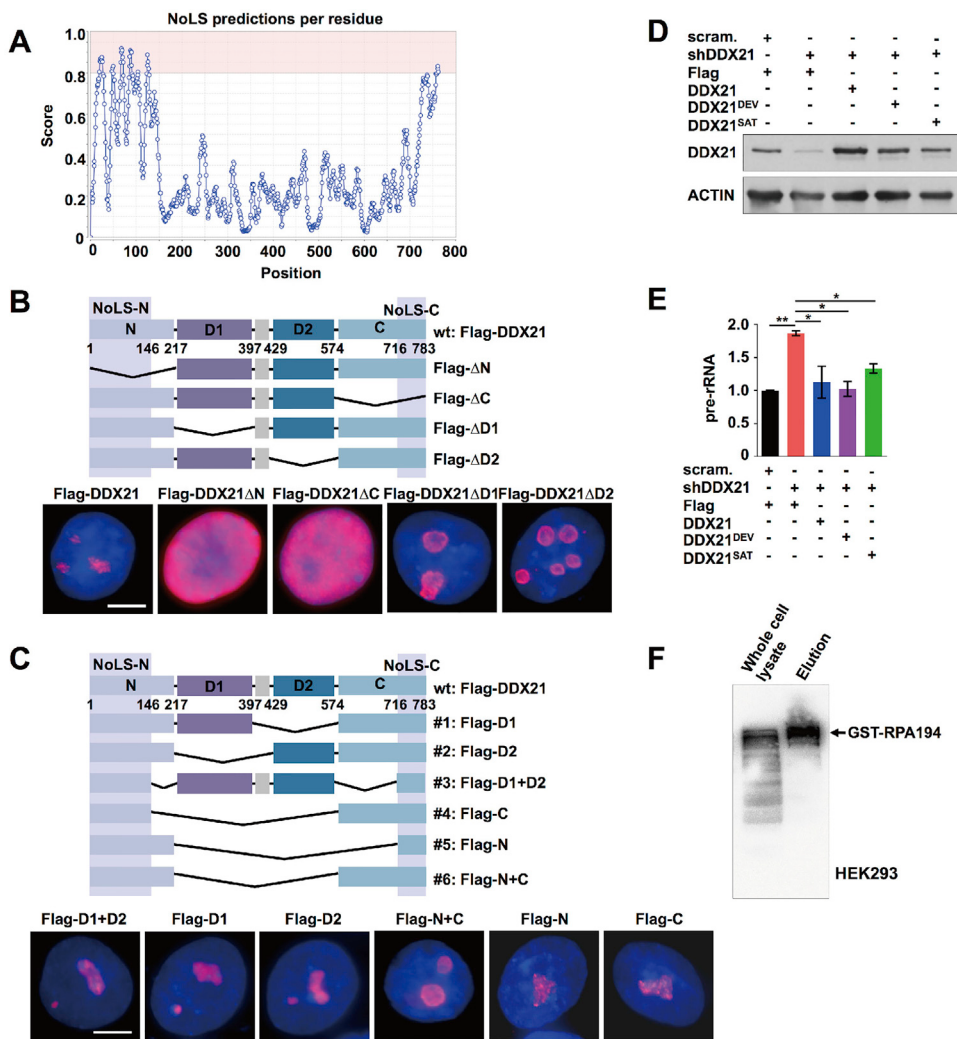


**Figure S7. The Nucleolar Location of DDX21 Requires NoLS in Both Its N-Terminal and C-Terminal Domains and DDX21 Helicase Activity Is Not Required for Pre-rRNA Transcription, Related to Figure 6**

(A) Prediction of NoLS in DDX21 by NoD (Nucleolar localization sequence Detector) (Scott et al., 2011). Four predicted NoLSs are located in the N- and C-terminal domains of DDX21: residues 19 and 45, residues 47 and 122, residues 124 and 146 and residues 761 and 782.

(B) DDX21 lacking of N- or C-terminal domain was distributed in the nucleoplasm. Top, the schematic drawing of DDX21 truncations. Bottom, IF of truncated DDX21 expressed in PA1 cells using anti-Flag antibodies. Scale bar, 5  $\mu$ m.

(C) DDX21 truncations with predicted NoLS were localized in the nucleolus. Top, the schematic drawing of DDX21 truncations fused with the N- and C-terminal NoLSs. Bottom, IF of DDX21 truncations expressed in PA1 cells using anti-Flag antibodies revealed that these truncations were all located to the nucleolus. Scale bar, 5  $\mu$ m.

(D and E) DDX21 helicase activity is not required for pre-rRNA transcription. The increased pre-rRNA production after DDX21 KD could be rescued by expression of wild-type DDX21, DDX21<sup>DEV</sup> or DDX21<sup>SAT</sup>. (D) western blotting revealed that the endogenous DDX21 depletion was rescued by transfection of DDX21 wild-type and two mutants to PA1 cells to similar levels by WB with anti-DDX21 antibodies. (E) The pre-rRNA expression in PA1 cells treated with different conditions in (D) was detected by qRT-PCR. Data were normalized to actin mRNA. Error bars represent SD in triplicate experiments.

(F) Purification of GST-RPA194 in HEK293 cells. The purified GST-RPA194 was revealed by WB with anti-GST antibodies.